

Chapter 14

Quantum discrete breathers

Ricardo A. Pinto¹ and Sergej Flach²

¹ Department of Electrical Engineering, University of California Riverside, Riverside, USA

² Max Planck Institute for the Physics of Complex Systems, Dresden, Germany

14.1 Introduction

In solid-state physics, the phenomenon of localization is usually perceived as arising from extrinsic disorder that breaks the discrete translational invariance of the perfect crystal lattice. Familiar examples include the localized vibrational modes around impurities or defects in crystals and Anderson localization of waves in disordered media [1]. The usual perception among solid-state researchers is that, in perfect lattices excitations must be extended objects as well, essentially plane wave like. Such firmly entrenched perceptions were severely jolted since the discovery of discrete breathers (DB), also known as intrinsic localized modes (ILM). These states are typical excitations in perfectly periodic but strongly nonlinear systems, and are characterized by being spatially localized, at variance to plane wave states [2–4].

DB-like excitations, being generic objects, have been observed in a large variety of lattice systems that include bond excitations in molecules, lattice vibrations and spin excitations in solids, charge flow in coupled Josephson junctions, light propagation in interacting optical waveguides, cantilever vibrations in micromechanical arrays, cold atom dynamics in Bose-Einstein condensates loaded on optical lattices, among others. They have been extensively studied, and a high level of understanding about their properties has been reached.

Two decades of intensive research have polished our theoretical understanding of DBs in classical nonlinear lattices. Less is known about their quantum counterparts - quantum breathers (QB). This chapter is devoted to a review of the more recent studies in this field. The concept of QBs is closely related with the theme of dynamical tunneling in phase space.

14.1.1 A few facts about classical discrete breathers

Let us study the combined effect of nonlinearity and discreteness on the spatial localization of a discrete breather on a basic level. For that we look into the dynamics of a one-dimensional chain of interacting (scalar) oscillators with the Hamiltonian

$$H = \sum_n \left[\frac{1}{2} p_n^2 + V(x_n) + W(x_n - x_{n-1}) \right]. \quad (14.1)$$

The integer n marks the lattice site number of a possibly infinite chain, and x_n and p_n are the canonically conjugated coordinate and momentum of a degree of freedom associated with site number n . The on-site potential V and the interaction potential W satisfy $V'(0) = W'(0) = 0$, $V''(0), W''(0) \geq 0$. This choice ensures that the classical ground state $x_n = p_n = 0$ is a minimum of the energy H . The equations of motion read

$$\dot{x}_n = p_n, \quad \dot{p}_n = -V'(x_n) - W'(x_n - x_{n-1}) + W'(x_{n+1} - x_n). \quad (14.2)$$

Let us linearize the equations of motion around the classical ground state. We obtain a set of linear coupled differential equations with solutions being small amplitude plane waves:

$$x_n(t) \sim e^{i(\omega_q t - qn)}, \quad \omega_q^2 = V''(0) + 4W''(0) \sin^2\left(\frac{q}{2}\right). \quad (14.3)$$

These waves are characterized by a wave number q and a corresponding frequency ω_q . All allowed plane wave frequencies fill a part of the real axis which is coined linear spectrum. Due to the underlying lattice the frequency ω_q depends periodically on q and its absolute value has always a *finite upper bound*. The maximum (Debye) frequency of small amplitude waves $\omega_\pi = \sqrt{V''(0) + 4W''(0)}$. Depending on the choice of the potential $V(x)$, ω_q can be either acoustic- or optic-like, $V(0) = 0$ and $V(0) \neq 0$, respectively. In the first case the linear spectrum covers the interval $-\omega_\pi \leq \omega_q \leq \omega_\pi$ which includes $\omega_{q=0} = 0$. In the latter case an additional (finite) gap opens for $|\omega_q|$ below the value $\omega_0 = \sqrt{V''(0)}$.

For large amplitude excitations the linearization of the equations of motion is not correct anymore. Similar to the case of a single anharmonic oscillator, the frequency of possible time-periodic excitations will depend on the amplitude of the excitation, and thus may be located outside the linear spectrum. Let us assume that a time-periodic and spatially localized state, i.e. a *discrete breather*, $\hat{x}_n(t + T_b) = \hat{x}_n(t)$ exists as an exact solution of Eqs.(14.2) with the period $T_b = 2\pi/\Omega_b$. Due to its time periodicity, we can expand $\hat{x}_n(t)$ into a Fourier series

$$\hat{x}_n(t) = \sum_k A_{kn} e^{ik\Omega_b t}. \quad (14.4)$$

The Fourier coefficients are by assumption also localized in space

$$A_{k,|n| \rightarrow \infty} \rightarrow 0. \quad (14.5)$$

Inserting this ansatz into the equations of motion (14.2) and linearizing the resulting algebraic equations for Fourier coefficients in the spatial breather tails (where the amplitudes are by assumption small) we arrive at the following linear algebraic equations:

$$k^2 \Omega_b^2 A_{kn} = V''(0) A_{kn} + W''(0) (2A_{kn} - A_{k,n-1} - A_{k,n+1}). \quad (14.6)$$

If $k\Omega_b = \omega_q$, the solution to (14.6) is $A_{k,n} = c_1 e^{iqn} + c_2 e^{-iqn}$. Any nonzero (whatever small) amplitude $A_{k,n}$ will thus oscillate without further spatial decay, contradicting the initial assumption. If however

$$k\Omega_b \neq \omega_q \quad (14.7)$$

for any integer k and any q , then the general solution to (14.6) is given by $A_{k,n} = c_1 \kappa^n + c_2 \kappa^{-n}$ where κ is a real number depending on ω_q , Ω_b and k . It always admits an (actually exponential) spatial decay by choosing either c_1 or c_2 to be nonzero. In order to fulfill (14.7) for at least one real value of Ω_b and any integer k , we have to request $|\omega_q|$ to be bounded from above. That is precisely the reason why the spatial lattice is needed. In contrast most spatially continuous field equations will have linear spectra which are unbounded. That makes resonances of higher order harmonics of a localized excitation with the linear spectrum unavoidable. The nonresonance condition (14.7) is thus an (almost) necessary condition for obtaining a time-periodic localized state on a Hamiltonian lattice [2].

The performed analysis can be extended to more general classes of discrete lattices, including e.g. long-range interactions between sites, more degrees of freedom per each site, higher-dimensional lattices etc. But the resulting non-resonance condition (14.7) keeps its generality, illustrating the key role of discreteness and nonlinearity for the existence of discrete breathers.

Let us show discrete breather solutions for various lattices. We start with a chain (14.1) with the functions

$$V(x) = x^2 + x^3 + \frac{1}{4}x^4, \quad W(x) = 0.1x^2. \quad (14.8)$$

The spectrum ω_q is optic-like and shown in Fig.14.1. Discrete breather solutions can have frequencies Ω_b which are located both below and above the linear spectrum. The time-reversal symmetry of (14.2) allows to search for DB displacements $x_n(t=0)$ when all velocities $\dot{x}_n(t=0) = 0$. These initial displacements are computed with high accuracy (see following sections) and plotted in the insets in Fig.14.1 [3]. We show solutions to two DB frequencies located above and below ω_q - their actual values are marked with the green arrows. To each DB frequency we show two different spatial DB patterns - among an infinite number of other possibilities, as we will see below. The high-frequency DBs ($\Omega_b \approx 1.66$) occur for large-amplitude, high-energy motion with adjacent particles moving out of phase. Low-frequency DBs ($\Omega_b \approx 1.26$) occur for small-amplitude motion with adjacent particles moving in phase.

In Fig.14.2 we show two DB solutions for a Fermi-Pasta-Ulam chain of particles coupled via anharmonic springs $V(x) = 0, W(x) = \frac{1}{2}x^2 + \frac{1}{4}x^4$ (c.f. (14.1)) which has an acoustic-type spectrum [5]. The DB frequency is in both cases $\Omega_b = 4.5$. Again the displacements x_n are shown for an initial time when all velocities vanish. In the inset we plot the strain $u_n = x_n - x_{n-1}$ on a log-normal scale. The DB solutions are exponentially localized in space.

Finally we show DB solutions for a *two-dimensional* square lattice of anharmonic oscillators with nearest neighbour coupling. The equations of motion read

$$\ddot{x}_{i,j} = k(x_{i+1,j} + x_{i-1,j} - 2x_{i,j}) + k(x_{i,j+1} + x_{i,j-1} - 2x_{i,j}) - x_{i,j} - x_{i,j}^3 \quad (14.9)$$

with oscillator potentials $V(x) = \frac{1}{2}x^2 + \frac{1}{4}x^4$. In Fig.14.3 we plot the oscillator displacements with all velocities equal to zero for three different DB frequencies and $k = 0.05$ [6]. For all cases adjacent oscillators move out of phase.

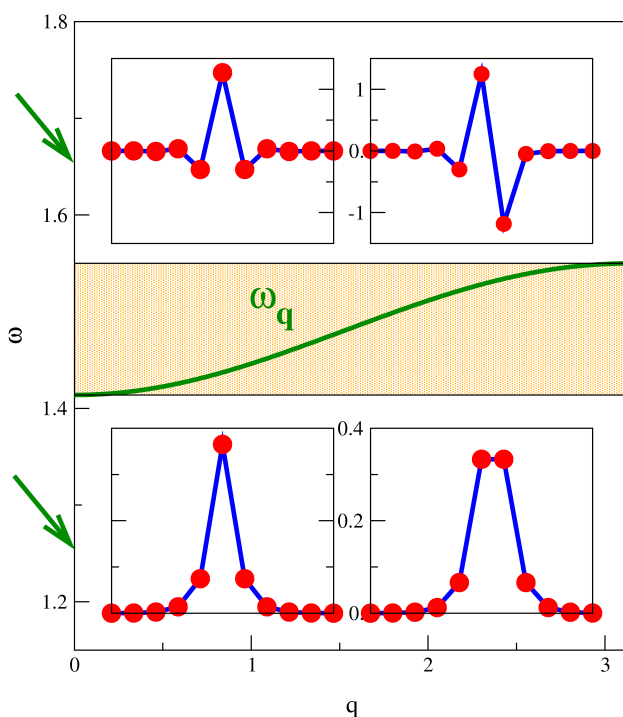


Figure 14.1: The frequency versus wavenumber dependence of the linear spectrum for a one-dimensional chain of anharmonic oscillators with potentials (14.8). Chosen DB frequencies are marked with green arrows and lie outside the linear spectrum ω_q . Red circles indicate the oscillator displacements for a given DB solution, with all velocities equal to zero. Lines connecting circles are guides for the eye. From [3].

We conclude this section with emphasizing that DB solutions can be typically localized on a few lattice sites, regardless of the lattice dimension. Thus little overall coherence is needed to excite a state nearby - just a few sites have to oscillate coherently, the rest of the lattice does not participate strongly in the excitation.

14.1.2 From classical to quantum

A natural question is what remains of discrete breathers if the corresponding quantum problem is considered [7–9]. The many-body Schrödinger equation is linear and translationally invariant, therefore all eigenstates must obey the Bloch theorem. Thus we cannot expect eigenstates of the Hamiltonian to be spatially localized (on the lattice). What is the correspondence between the quantum eigenvalue problem and the classical dynamical evolution?

The concept of tunneling is a possible answer to this puzzle. Naively speaking we quantize the family of periodic orbits associated with a discrete breather located somewhere on the lattice. Notice that there are as many such families as there are lattice sites. The quantization (e.g., Bohr-Sommerfeld) yields some eigenvalues. Since we can perform the same procedure with any family of discrete breather periodic orbits which differ only in their location on the lattice, we obtain N -fold degeneracy for every thus obtained eigenvalue, where N stands for the number of lattice sites. Unless we consider the trivial case of uncoupled lattice sites, these

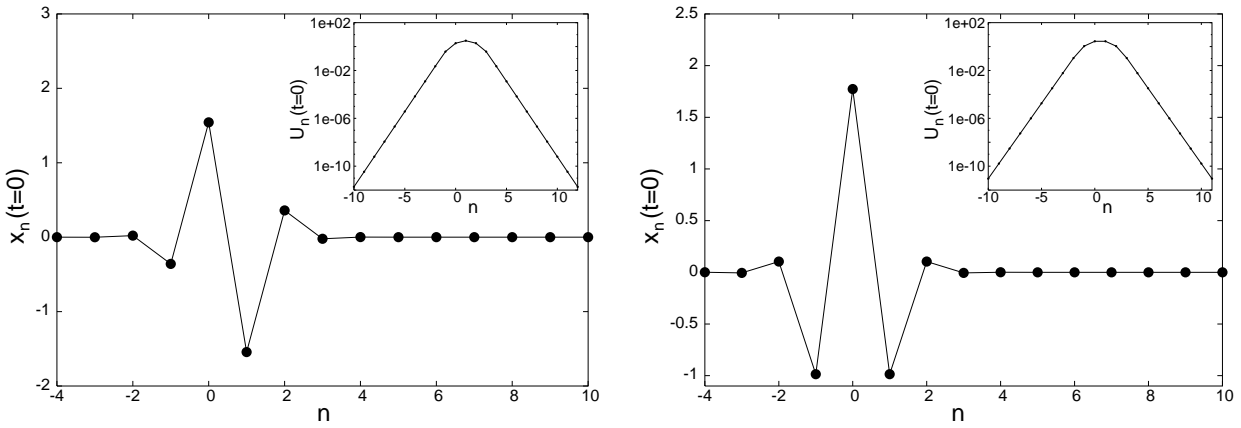


Figure 14.2: Discrete breather solutions for a Fermi-Pasta-Ulam chain (see text). These states are frequently referred to as the Page mode (left) and the Sievers-Takeno mode (right). Adapted from [5].

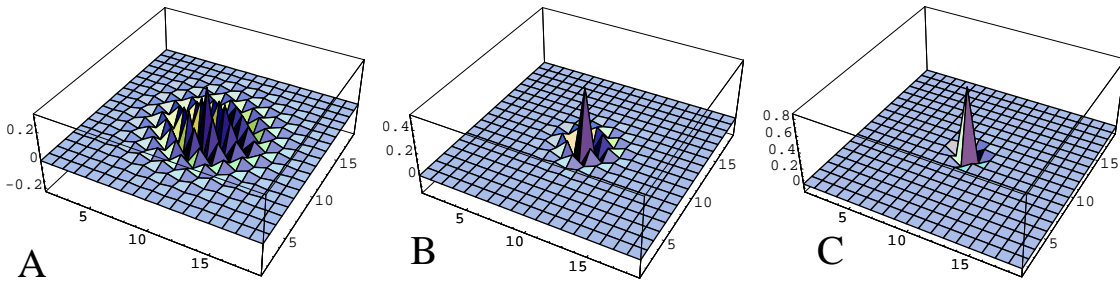


Figure 14.3: Displacements of DBs on a two-dimensional lattice (14.9) with $k = 0.05$, all velocities equal to zero. (A) $\Omega_b = 1.188$; (B) $\Omega_b = 1.207$; (C) $\Omega_b = 1.319$. From [6].

degeneracies will be lifted. Consequently, we will instead obtain bands of states with finite band width. These bands will be called quantum breather bands. The inverse tunneling time of a semiclassical breather from one site to a neighboring one is a measure of the bandwidth.

We can then formulate the following expectation: if a classical nonlinear Hamiltonian lattice possesses discrete breathers, its quantum counterpart should show up with nearly degenerate bands of eigenstates, if the classical limit is considered. The number of states in such a band is N , and the eigenfunctions are given by Bloch-like superpositions of the semiclassical eigenfunctions obtained using the mentioned Bohr-Sommerfeld quantization of the classical periodic orbits. By nearly degenerate we mean that the bandwidth of a quantum breather band is much smaller than the spacing between different breather bands and the average level spacing in the given energy domain, and the classical limit implies large eigenvalues.

Another property of a quantum breather state is that such a state shows up with exponential localization in appropriate correlation functions [10]. This approach selects all many-particle bound states, no matter how deep one is in the quantum regime. In this sense quantum breather states belong to the class of many-particle bound states.

For large energies and N the density of states becomes large too. What will happen to the expected quantum breather bands then? Will the hybridization with other non-breather states destroy the particle-like nature of the quantum breather, or not? What is the impact of the nonintegrability of most systems allowing for classical breather solutions? Since the quantum case corresponds to a quantization of the classical phase space, we could expect that chaotic trajectories lying nearby classical breather solutions might affect the corresponding quantum eigenstates.

From a computational point of view we are very much restricted in our abilities to study quantum breathers. Ideally we would like to study quantum properties of a lattice problem in the high energy domain (to make contact with classical states) and for large lattices. This is typically impossible, since solving the quantum problem amounts to diagonalizing the Hamiltonian matrix with rank b^N where b is the number of states per site, which should be large to make contact with classical dynamics. Thus typically quantum breather states have been so far obtained numerically for small one-dimensional systems [10–12].

14.2 Quantum breather models

14.2.1 The Bose-Hubbard chain

Let us discuss quantum breathers within the widely used quantum discrete nonlinear Schrödinger model (also called Bose-Hubbard model) with the Hamiltonian [13]

$$H = - \sum_{l=1}^N \left[\frac{1}{2} a_l^\dagger a_l^\dagger a_l a_l + C(a_l^\dagger a_{l+1} + h.c.) \right] \quad (14.10)$$

and the commutation relations

$$a_l a_m^\dagger - a_m^\dagger a_l = \delta_{lm} \quad (14.11)$$

with δ_{lm} being the standard Kronecker symbol. This Hamiltonian conserves the total number of particles

$$B = \sum_l n_l, \quad n_l = a_l^\dagger a_l. \quad (14.12)$$

For b particles and N sites the number of basis states is

$$\frac{(b + N - 1)!}{b!(N - 1)!}. \quad (14.13)$$

For $b = 0$ there is just one trivial state of an empty lattice. For $b = 1$ there are N states which correspond to one-boson excitations. These states are similar to classical extended wave states. For $b = 2$ the problem is still exactly solvable, because it corresponds to a two-body problem on a lattice. A corresponding numerical solution is sketched in Fig. 14.4.

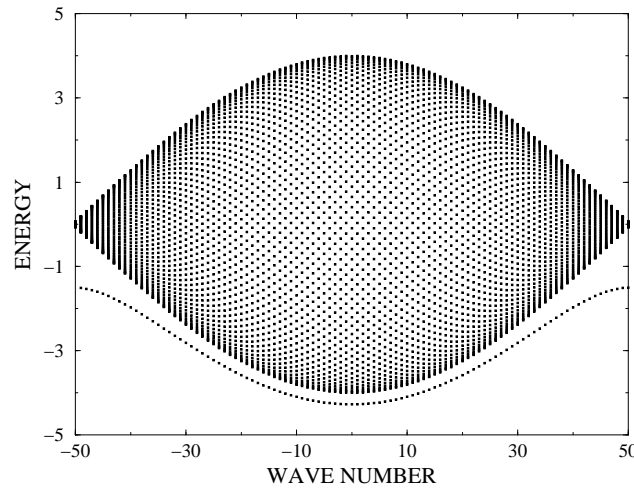


Figure 14.4: Spectrum of the quantum DNLS with $b = 2$ and $N = 101$. The energy eigenvalues are plotted versus the wavenumber of the eigenstate. Adapted from [13].

Note the wide two-particle continuum, and a single band located below. This single band corresponds to quasiparticle states characterized by one single quantum number (related to the wavenumber q). These states are two-particle bound states. The dispersion of this band is given [13] by

$$E = -\sqrt{1 + 16C^2 \cos^2\left(\frac{q}{2}\right)}. \quad (14.14)$$

Any eigenstate from this two-particle bound state band is characterized by exponential localization of correlations, i.e. when represented in some set of basis states, the amplitude or overlap with a basis state where the two particles are separated by some number of sites is exponentially decreasing with increasing separation distance. Note that a compact bound state is obtained for $q = \pm\pi$, i.e. for these wave numbers basis states with nonzero separation distance do not contribute to the eigenstate at all [14].

14.2.2 The dimer

A series of papers was devoted to the properties of the quantum dimer [15–18]. This system describes the dynamics of bosons fluctuating between two sites. The number of bosons is conserved, and together with the conservation of energy the system appears to be integrable. Of course, one cannot consider spatial localization in such a model. However, a reduced form of the discrete translational symmetry - namely the permutational symmetry of the two sites - can be imposed. Together with the addition of nonlinear terms in the classical equations of motion the dimer allows for classical trajectories which are not invariant under permutation. The phase space can be completely analyzed, all isolated periodic orbits (IPO) can be found. There appears exactly one bifurcation on one family of isolated periodic orbits, which leads to the appearance of a separatrix in phase space. The separatrix separates three regions - one invariant and two non-invariant under permutations. The subsequent analysis of the quantum dimer demonstrated the existence of pairs of eigenstates with nearly equal eigenenergies [15]. The separatrix and the bifurcation in the classical phase space can be traced in the spectrum of the quantum dimer [17].

The classical Hamiltonian may be written as

$$H = \Psi_1^* \Psi_1 + \Psi_2^* \Psi_2 + \frac{1}{2} \left((\Psi_1^* \Psi_1)^2 + (\Psi_2^* \Psi_2)^2 \right) + C (\Psi_1^* \Psi_2 + \Psi_2^* \Psi_1) . \quad (14.15)$$

with the equations of motion $\dot{\Psi}_{1,2} = i\partial H/\partial \Psi_{1,2}^*$. The model conserves the norm (or number of particles) $B = |\Psi_1|^2 + |\Psi_2|^2$.

Let us parameterize the phase space of (14.15) with $\Psi_{1,2} = A_{1,2} e^{i\phi_{1,2}}$, $A_{1,2} \geq 0$. It follows that $A_{1,2}$ is time independent and $\phi_1 = \phi_2 + \Delta$ with $\Delta = 0, \pi$ and $\dot{\phi}_{1,2} = \omega$ being also time independent. Solving the algebraic equations for the amplitudes of the IPOs we obtain

$$\text{I} : A_{1,2}^2 = \frac{1}{2} B , \quad \Delta = 0 , \quad \omega = 1 + C + \frac{1}{2} B , \quad (14.16)$$

$$\text{II} : A_{1,2}^2 = \frac{1}{2} B , \quad \Delta = \pi , \quad \omega = 1 - C + \frac{1}{2} B , \quad (14.17)$$

$$\text{III} : A_1^2 = \frac{1}{2} B \left(1 \pm \sqrt{1 - 4C^2/B^2} \right) , \quad \Delta = 0 , \quad \omega = 1 + B . \quad (14.18)$$

IPO III corresponds to two elliptic solutions which break the permutational symmetry. IPO III exists for $B \geq B_b$ with $B_b = 2C$ and occurs through a bifurcation from IPO I. The corresponding separatrix manifold is uniquely defined by the energy of IPO I at a given value of $B \geq B_b$. This manifold separates three regions in phase space - two with symmetry broken solutions, each one containing one of the IPOs III, and one with symmetry conserving solutions containing the elliptic IPO II. The separatrix manifold itself contains the hyperbolic IPO I. For $B \leq B_b$ only two IPOs exist - IPO I and II, with both of them being of elliptic character. Remarkably there exist no other IPOs, and the mentioned bifurcation and separatrix manifolds are the only ones present in the classical phase space of (14.15).

To conclude the analysis of the classical part, we list the energy properties of the different phase space parts separated by the separatrix manifold. First it is straightforward to show that the IPOs (14.16)-(14.18) correspond to maxima, minima or saddle points of the energy in the allowed energy interval for a given value of B , with no other extrema or saddle points

present. It follows

$$E_1 = H(\text{IPO I}) = B + \frac{1}{4}B^2 + CB \quad , \quad (14.19)$$

$$E_2 = H(\text{IPO II}) = B + \frac{1}{4}B^2 - CB \quad , \quad (14.20)$$

$$E_3 = H(\text{IPO III}) = B + \frac{1}{2}B^2 + C^2 \quad . \quad (14.21)$$

For $B < B_b$ we have $E_1 > E_2$ (IPO I - maximum, IPO II - minimum). For $B \geq B_b$ it follows $E_3 > E_1 > E_2$ (IPO III - maxima, IPO I - saddle, IPO II - minimum). If $B < B_b$, then all trajectories are symmetry conserving. If $B \geq B_b$, then trajectories with energies $E_1 < E \leq E_3$ are symmetry breaking, and trajectories with $E_2 \leq E \leq E_1$ are symmetry conserving.

The quantum eigenvalue problem amounts to replacing the complex functions Ψ, Ψ^* in (14.15) by the boson annihilation and creation operators a, a^\dagger with the standard commutation relations (to enforce the invariance under the exchange $\Psi \Leftrightarrow \Psi^*$ the substitution has to be done on rewriting $\Psi\Psi^* = 1/2(\Psi\Psi^* + \Psi^*\Psi)$):

$$H = \frac{5}{4} + \frac{3}{2} \left(a_1^\dagger a_1 + a_2^\dagger a_2 \right) + \frac{1}{2} \left((a_1^\dagger a_1)^2 + (a_2^\dagger a_2)^2 \right) + C \left(a_1^\dagger a_2 + a_2^\dagger a_1 \right) \quad . \quad (14.22)$$

Note that $\hbar = 1$ here, and the eigenvalues b of $B = a_1^\dagger a_1 + a_2^\dagger a_2$ are integers. Since B commutes with H we can diagonalize the Hamiltonian in the basis of eigenfunctions of B . Each value of b corresponds to a subspace of the dimension $(b+1)$ in the space of eigenfunctions of B . These eigenfunctions are products of the number states $|n\rangle$ of each degree of freedom and can be characterized by a symbol $|n, m\rangle$ with n bosons in the site 1 and m bosons in the site 2. For a given value of b it follows $m = b - n$. So we can actually label each state by just one number n : $|n, (b-n)\rangle \equiv |n\rangle$. Consequently the eigenvalue problem at fixed b amounts to diagonalizing the matrix

$$H_{nm} = \begin{cases} \frac{5}{4} + \frac{3}{2}b + \frac{1}{2}(n^2 + (b-n)^2) & n = m \\ C\sqrt{n(b+1-n)} & n = m + 1 \\ C\sqrt{(n+1)(b-n)} & n = m - 1 \\ 0 & \text{else} \end{cases} \quad (14.23)$$

where $n, m = 0, 1, 2, \dots, b$. Notice that the matrix H_{nm} is a symmetric band matrix. The additional symmetry $H_{nm} = H_{(b-n), (b-m)}$ is a consequence of the permutational symmetry of H . For $C = 0$ the matrix H_{nm} is diagonal, with the property that each eigenvalue is doubly degenerate (except for the state $|b/2\rangle$ for even values of b). The classical phase space contains only symmetry broken trajectories, with the exception of IPO II and the separatrix with IPO I (in fact in this limit the separatrix manifold is nothing but a resonant torus containing both IPOs I and II). With the exception of the separatrix manifold, all tori break permutational symmetry and come in two groups separated by the separatrix. Then quantizing each group will lead to pairs of degenerate eigenvalues - one from each group. There is a clear correspondence to the spectrum of the diagonal ($C = 0$) matrix H_{nm} . The eigenvalues $H_{00} = H_{bb}$ correspond to the quantized IPOs III. With increasing n the eigenvalues $H_{nn} = H_{(b-n), (b-n)}$ correspond to quantized tori further away from the IPO III. Finally the states with $n = b/2$ for even b or $n = (b-1)/2$ for odd b are tori most close to the separatrix. Switching the side diagonals on by increasing C will lead to

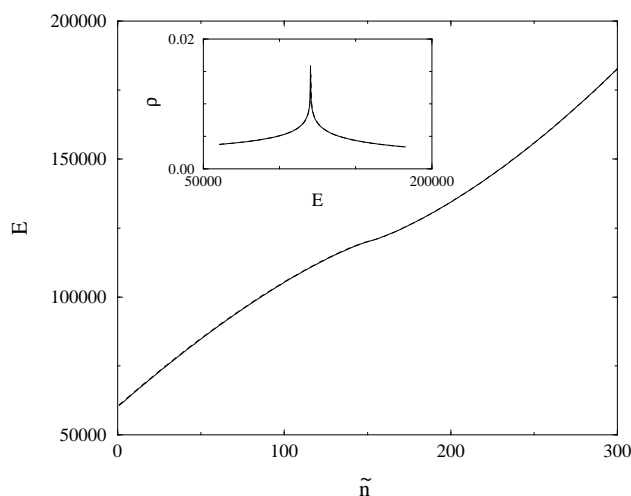


Figure 14.5: Eigenvalues versus ordered state number \tilde{n} for symmetric and antisymmetric states ($0 < \tilde{n} < b/2$ for both types of states). Parameters: $b = 600$ and $C = 50$. Inset: Density of states versus energy. Adapted from [17].

a splitting of all pairs of eigenvalues. In the case of small values of b these splittings have no correspondence to classical system properties. However, in the limit of large b we enter the semiclassical regime, and due to the integrability of the system, eigenfunctions should correspond to tori in the classical phase space which satisfy the Einstein-Brillouin-Keller quantization rules. Increasing C from zero will lead to a splitting ΔE_n of the eigenvalue doublets of $C = 0$. In other words, we find pairs of eigenvalues, which are related to each other through the symmetry of their eigenvectors and (for small enough C) through the small value of the splitting. These splittings have been calculated numerically and using perturbation theory [15,17]. In the limit of large b the splittings are exponentially small for energies above the classical separatrix energy (i.e. for classical trajectories which are not invariant under permutation). If the eigenenergies are lowered below the classical separatrix energy, the splittings grow rapidly up to the mean level spacing.

In Fig. 14.5 the results of a diagonalization of a system with 600 particles ($b = 600$) is shown [17]. The inset shows the density of states versus energy, which nicely confirms the predicted singularity at the energy of the separatrix of the classical counterpart. In order to compute the exponentially small splittings, we may use e.g. a Mathematica routine which allows to choose arbitrary values for the precision of computations. Here we chose precision 512. In Fig. 14.6 the numerically computed splittings are compared to perturbation theory results. As expected, the splittings become extremely small above the separatrix. Consequently these states will follow for long times the dynamics of a classical broken symmetry state.

14.2.3 The trimer

The integrability of the dimer does not allow a study of the influence of chaos (i.e. non-integrability) on the tunneling properties of the mentioned pairs of eigenstates. A natural extension of the dimer to a trimer adds a third degree of freedom without adding a new integral of motion. Consequently the trimer is nonintegrable. A still comparatively simple

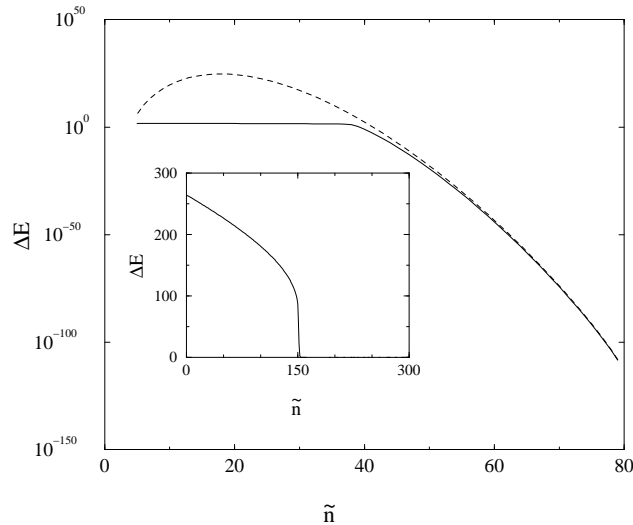


Figure 14.6: Eigenvalue splittings versus \tilde{n} for $b = 150$ and $C = 10$. Solid line - numerical result, dashed line - perturbation theory. Inset: Same for $b = 600$ and $C = 50$. Only numerical results are shown. Adapted from [17].

numerical quantization of the trimer allows to study the behavior of many tunneling states in the large-energy domain of the eigenvalue spectrum [19].

Similarly to the dimer, the quantum trimer Hamiltonian is represented in the form

$$H = \frac{15}{8} + \frac{3}{2}(a_1^\dagger a_1 + a_2^\dagger a_2 + a_3^\dagger a_3) + \frac{1}{2} \left[(a_1^\dagger a_1)^2 + (a_2^\dagger a_2)^2 \right] + C(a_1^\dagger a_2 + a_2^\dagger a_1) + \delta(a_1^\dagger a_3 + a_3^\dagger a_1 + a_2^\dagger a_3 + a_3^\dagger a_2) . \quad (14.24)$$

Again $B = a_1^\dagger a_1 + a_2^\dagger a_2 + a_3^\dagger a_3$ commutes with the Hamiltonian, thus we can diagonalize (14.24) in the basis of eigenfunctions of B . For any finite eigenvalue b of B the number of states is finite, namely $(b+1)(b+2)/2$. Thus the infinite dimensional Hilbert space separates into an infinite set of finite dimensional subspaces, each subspace containing only vectors with a given eigenvalue b . These eigenfunctions are products of the number states $|n\rangle$ of each degree of freedom and can be characterized by a symbol $|n, m, l\rangle$ where we have n bosons on site 1, m bosons on site 2, and l bosons on site 3. For a given value b it follows that $l = b - m - n$. So we can actually label each state by just two numbers (n, m) : $|n, m, (b - n - m)\rangle \equiv |n, m\rangle$. Note that the third site added to the dimer is different from the first two sites. There is no boson-boson interaction on this site. Thus site 3 serves simply as a boson reservoir for the dimer. Dimer bosons may now fluctuate from the dimer to the reservoir. The trimer has the same permutational symmetry as the dimer.

The matrix elements of (14.24) between states from different b subspaces vanish. Thus for any given b the task amounts to diagonalizing a finite dimensional matrix. The matrix has a tridiagonal block structure, with each diagonal block being a dimer matrix (14.23). The nonzero off-diagonal blocks contain interaction terms proportional to δ . We consider symmetric $|\Psi\rangle_s$ and antisymmetric $|\Psi\rangle_a$ states. The structure of the corresponding symmetric and antisymmetric decompositions of H is similar to H itself. In the following we will present results for $b = 40$. We will also drop the first two terms of the RHS in (14.24), because these only lead to a shift of the energy spectrum. Since we evaluate the matrix elements explic-

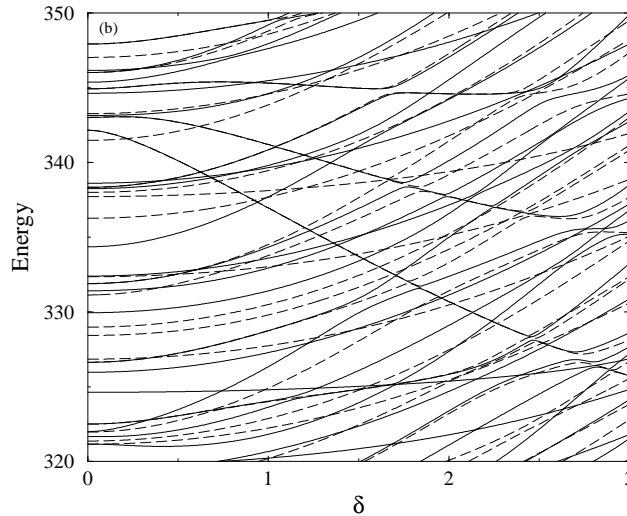


Figure 14.7: A part of the eigenenergy spectrum of the quantum trimer as a function of δ with $b = 40$ and $C = 2$. Lines connect data points for a given state. Solid lines - symmetric eigenstates; thick dashed lines - antisymmetric eigenstates. Adapted from [19].

itly, we need only a few seconds to obtain all eigenvalues and eigenvectors with the help of standard Fortran routines. In Fig. 14.7 we plot a part of the energy spectrum as a function of δ for $C = 2$ [19]. As discussed above, the Hamiltonian decomposes into noninteracting blocks for $\delta = 0$, each block corresponding to a dimer with a boson number between 0 and b . For $\delta \neq 0$ the block-block interaction leads to typical features in the spectrum, like, e.g., avoided crossings. The full quantum energy spectrum extends roughly over 10^3 , leading to an averaged spacing of order 10^0 . Also the upper third of the spectrum is diluted compared to the lower two thirds. The correspondence to the classical model is obtained with the use of the transformation $E_{cl} = E_{qm}/b^2 + 1$ and for parameters C/b and δ/b (the classical value for B is $B = 1$).

The main result of this computation so far is that tunneling pairs of eigenstates of the dimer persist in the nonintegrable regime $\delta \neq 0$. However at certain pair-dependent values of δ a pair breaks up. From the plot in Fig. 14.7 we cannot judge how the pair splittings behave. In Fig. 14.8 we plot the pair splitting of the pair which has energy ≈ 342 at $\delta = 0$ [20]. Denote with x, y, z the eigenvalues of the site number operators n_1, n_2, n_3 . We may consider the quantum states of the trimer at $\delta = 0$ when z is a good quantum number and then follow the evolution of these states with increasing δ . The state for $\delta = 0$ can be traced back to $C = 0$ and be thus characterized in addition by x and y . The chosen pair states are then characterized by $x = 26(0)$, $y = 0(26)$ and $z = 14$ for $C = \delta = 0$. Note that this pair survives approximately 30 avoided crossings before it is finally destroyed at coupling strength $\delta \approx 2.67$ as seen in Fig. 14.7.

From Fig. 14.8 we find that the splitting rapidly increases gaining about eight orders of magnitude when δ changes from 0 to slightly above 0.5. Then this rapid but nevertheless smooth rise is interrupted by very sharp spikes when the splitting ΔE rises by several orders of magnitude with δ changing by mere percents and then abruptly changes in the opposite direction sometimes even overshooting its pre-spike value. Such spikes, some larger, some smaller, repeat with increasing δ until the splitting value approaches the mean level spacing

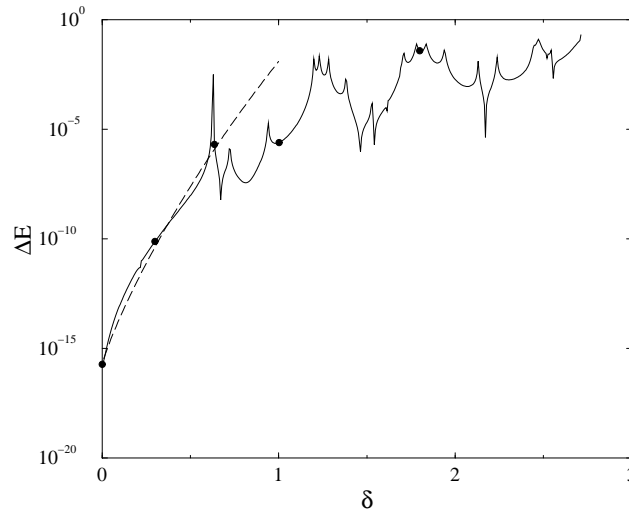


Figure 14.8: Level splitting versus δ for a level pair as described in the text. Solid line - numerical result. Dashed line - semiclassical approximation. Filled circles - location of wave function analysis in Fig. 14.9. Adapted from [20].

of order one. Only then one may say that the pair is destroyed since it can be hardly distinguished among the other trimer levels.

Another observation is presented in Fig. 14.9 [20]. We plot the intensity distribution of the logarithm of the squared symmetric wave function of our chosen pair for five different values of $\delta = 0, 0.3, 0.636, 1.0, 1.8$ (their locations are indicated by filled circles in Fig. 14.8). We use the eigenstates of B as basis states. They can be represented as $|x, y, z\rangle$ where x, y, z are the particle numbers on sites 1, 2, 3, respectively. Due to the commutation of B with H two site occupation numbers are enough if the total particle number is fixed. Thus the final encoding of states (for a given value of b) can be chosen as $|x, z\rangle$. The abscissa in Fig. 14.9 is x and the ordinate is z . Thus the intensity plots provide us with information about the order of particle flow in the course the tunneling process. For $\delta = 0$ (Fig. 14.9(a)) the only possibility for the 26 particles on site 1 is to directly tunnel to site 2. Site 3 is decoupled with its 14 particles not participating in the process. The squared wave function takes the form of a compact rim in the (x, z) plane which is parallel to the x axis. Nonzero values of the wave function are observed only on the rim. This direct tunneling has been described in chapter 14.2.2. When switching on some nonzero coupling to the third site, the particle number on the dimer (sites 1,2) is not conserved anymore. The third site serves as a particle reservoir which is able either to collect particles from or supply particles to the dimer. This coupling will allow for nonzero values of the wave function away from the rim. But most importantly, it will change the shape of the rim. We observe that the rim is bended down to smaller z values with increasing δ . That implies that the order of tunneling (when, e.g., going from large to small x values) is as follows: first, some particles tunnel from site 1 to site 2 and simultaneously from site 3 to site 2 (Fig. 14.10(a)). Afterwards particles flow from site 1 to both sites 2 and 3 (Fig. 14.10(b)). With increasing δ the structure of the wave function intensity becomes more and more complex, possibly revealing information about the classical phase space flow structure. Thus we observe three intriguing features. First, the tunneling splitting increases by eight orders of magnitude when δ increases from zero to 0.5. This seems to be unexpected, since at those values perturbation theory in δ should be applicable (at least Fig. 14.7 indicates that this should be true for the levels themselves).

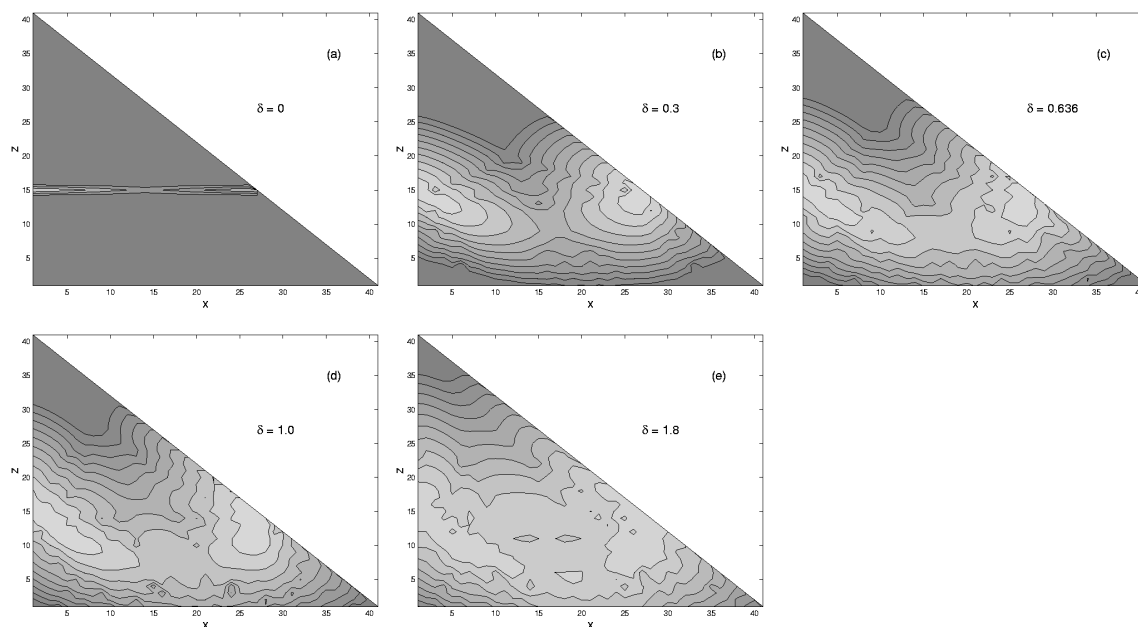


Figure 14.9: Contour plot of the logarithm of the symmetric eigenstate of the chosen tunneling pair (cf. Fig. 14.7) for five different values of $\delta = 0, 0.3, 0.636, 1.0, 1.8$ (their location is indicated by filled circles in Fig. 14.8). (a): three equidistant grid lines are used; (b-e): ten grid lines are used. Minimum value of squared wave function is 10^{-30} , maximum value is about 1. Adapted from [20].

The semiclassical explanation of this result was obtained in [20].

The second observation is that the tunneling begins with a flow of particles from the bath (site 3) directly to the empty site which is to be filled (with simultaneous flow from the filled dimer site to the empty one). At the end of the tunneling process the initially filled dimer site is giving particles back to the bath site. Again this is an unexpected result, since it implies that the particle number on the dimer is increasing during the tunneling, which seems to decrease the tunneling probability, according to the results for an isolated dimer. These first two results are closely connected (see [20] for a detailed explanation).

The third result concerns the resonant structure on top of the smooth variation in Fig. 14.8. The resonant enhancements and suppressions of tunneling are related to avoided crossings. Their presence implies that a fine tuning of the system parameters may strongly suppress or enhance tunneling which may be useful for spectroscopic devices. In Fig. 14.11 we show the four various possibilities of avoided crossings between a pair and a single level and between two pairs, and the schematic outcome for the tunneling splitting [20]. If the interaction to further more distant states in the spectrum is added, the tunneling splitting can become exactly zero [21] for some specific value of the control parameter. In such a rare situation the tunneling is suppressed for all times.

14.2.4 Quantum roto-breathers

When discussing classical breather solutions we have been touching some aspects of roto-breathers, including their property of being not invariant under time reversal symmetry. In

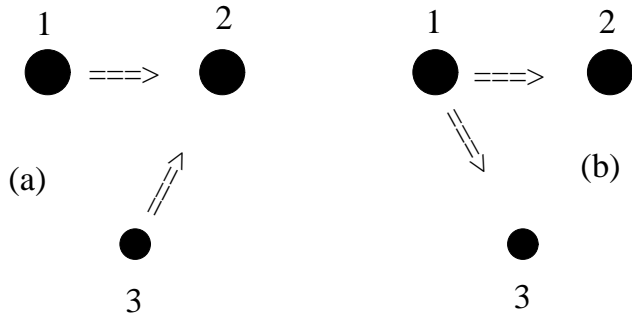


Figure 14.10: Order of tunneling in the trimer. Filled large circles - sites 1 and 2, filled small circle - site 3. Arrows indicate direction of transfer of particles. Adapted from [20].

a recent study Dorignac et al have performed [22] an analysis of the corresponding quantum roto-breather properties in a dimer with the Hamiltonian

$$H = \sum_{i=1}^2 \left\{ \frac{p_i^2}{2} + \alpha(1 - \cos x_i) \right\} + \varepsilon(1 - \cos(x_1 - x_2)). \quad (14.25)$$

The classical roto-breather solution consists of one pendulum rotating and the other oscillating with a given period T_b . Since the model has two symmetries - permutation of the indices and time-reversal symmetry - which may be both broken by classical trajectories, the irreducible representations of quantum eigenstates contain four symmetry sectors (with possible combinations of symmetric or antisymmetric states with respect to the two symmetry operations). Consequently, a quantum roto-breather state is belonging to a quadruplet of weakly split states rather than to a pair as discussed above. The schematic representation of the appearance of such a quadruplet is shown in Fig. 14.12 [22]. The obtained quadruplet has an additional fine structure as compared to the tunneling pair of the above considered dimer and trimer. The four levels in the quadruplet define three characteristic tunneling processes. Two of them are energy or momentum transfer from one pendulum to the other one, while the third one corresponds to total momentum reversal (which restores time reversal symmetry). The dependence of the corresponding tunneling rates on the coupling ε is shown for a specific quadruplet from [22] in Fig. 14.13. For very weak coupling $\varepsilon \ll 1$ the fastest tunneling process will be momentum reversal, since tunneling between the pendula is blocked. However as soon as the coupling is increased, the momentum reversal turns into the slowest process, with breather tunneling from one pendulum to the other one being orders of magnitude faster. Note that again resonant features on these splitting curves are observed, which are related to avoided crossings.

14.2.5 Large lattices with fluctuating numbers of quanta

A number of publications are devoted to the properties of quantum breathers in chains and two-dimensional lattices of coupled anharmonic oscillators. For the respective one-dimensional case, the Hamiltonian is given by

$$H = \sum_n \left[\frac{1}{2} p_n^2 + V(x_n) + W(x_n - x_{n-1}) \right]. \quad (14.26)$$

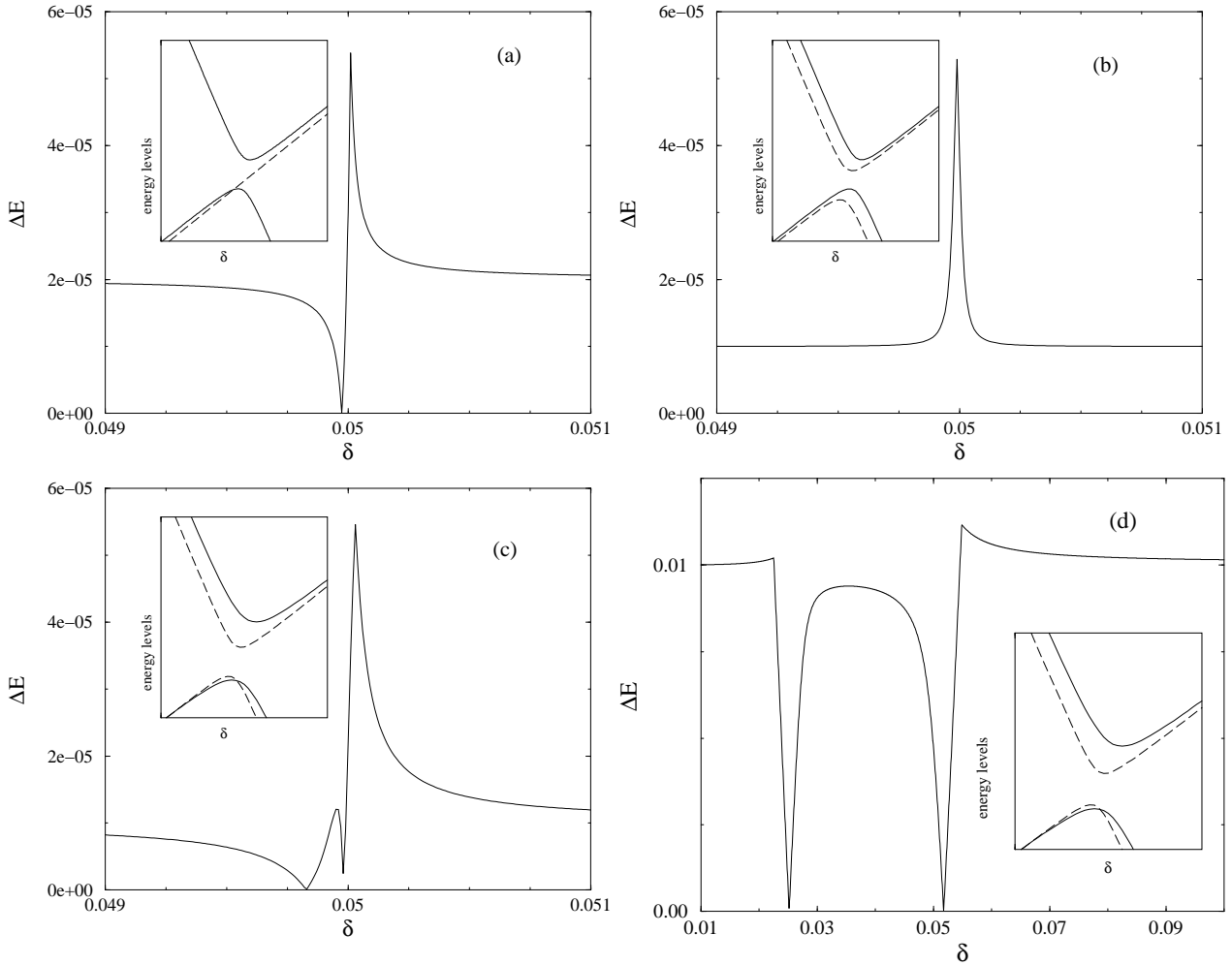


Figure 14.11: Level splitting variation at avoided crossings. Inset: Variation of individual eigenvalues participating in the avoided crossing. Solid lines - symmetric eigenstates, dashed lines - antisymmetric eigenstates. Adapted from [20].

Here $V(x) = \frac{1}{2}x^2 + \frac{1}{4}v_4x^4$ (or similar) and the nearest neighbour coupling $W(x) = \frac{1}{2}Cx^2$. The classical version of such models conserves only the energy, but not any equivalent of a norm. Therefore, no matter whether one uses creation and annihilation operators of the harmonic oscillator [23], or similar operators which diagonalize the single anharmonic oscillator problem [24], the resulting Hamiltonian matrix will not commute with the corresponding number operator. Calculations will typically be restricted to 4-6 quanta, and lattice sizes of the order of 30 for $d = 1$, 13×13 for $d = 2$ [23]. With these parameters one can calculate properties of quantum breather states, which correspond to typically two quanta which are bound (with unavoidable states with different number of quanta, contributing as well). For large enough v_4 a complete gap opens between the two-quanta continuum and quantum breather states [10, 23] (Figs.14.14 and 14.15). When decreasing the anharmonic constant v_4 , Provile found, that the gap closes for certain wave numbers, but persists for others, becoming a pseudogap [23, 25] (Fig.14.14).

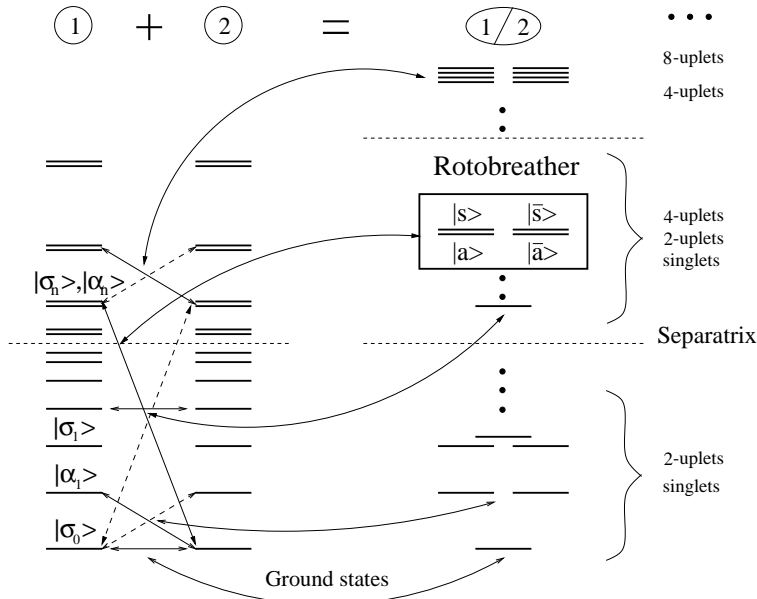


Figure 14.12: Schematic representation of the sum of two pendula spectra. Straight solid arrows indicate the levels to be added and dashed arrows the symmetric (permutation) operation. The result is indicated in the global spectrum by a curved arrow. The construction of the quantum roto-breather state is explicitly represented. Adapted from [22].

Involved calculations of the dynamical structure factor (e.g. available by neutron scattering in crystals) have shown, that signatures of quantum breathers are imprinted in these integral characteristics of the underlying lattice dynamics [10, 24], yet the working out of these differences may become a subtle task (see Fig.14.16 for an example).

Finally, Fleurov et al [26] estimated the influence of the tunnel splitting of a dimer, when embedded in an infinite chain. This situation is close to the tunneling of a very localized DB, so that the nonlinearity (interaction between bosons) can be taken into account only on the two sites, which participate in the tunneling, while the nonlinearity can be neglected on all other sites. Using path integral techniques, the computed tunneling splitting has been shown to become smaller as compared to the case of an isolated dimer. This is due to the fact, that a DB in an infinite chain has a core and a localized tail. That tail has to be carried through the tunneling process as well, and in analogy with a single particle tunneling in a double well, the tail increases the effective mass of such a particle. Consequently the exponential tail of a DB in an infinite chain tends to decrease its ability to perform quantum tunneling motion, yet it never leads to a full suppression of tunneling [26].

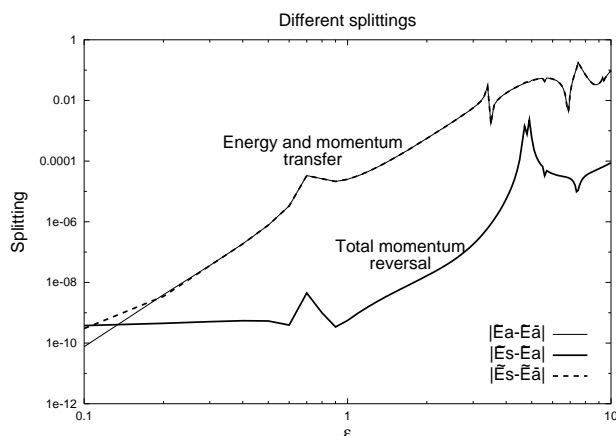


Figure 14.13: Dependence of different splittings of a quadruplet on ε . Only three of them have been displayed, each being associated with a given tunneling process. Adapted from [22].

14.3 Quantum breather properties

14.3.1 Evolution of quantum localized states

Suppose that we initially excite only one site in the trimer from above. If this initial state has strong enough overlap with tunneling pair eigenstates, its evolution in time should show distinct properties as compared to the case when the overlap is vanishing, or when there are simply no tunneling pair states available. Several results have been reported. First, a quantum echo was observed in [19] by calculating the survival probability of the initial state as a function of time. That quantity measures the probability to find the system in the initial state at later times. If the initial state has strong overlap with many eigenstates, it is expected to quickly decohere into these different states. Yet, if a substantial overlap with quantum breathers takes place, the survival probability first rapidly decays to zero, but echoes up after regular time intervals (Fig.14.17, left plot). If one simply measures the dependence of the number of quanta, then a similar situation will show up with a very slow beating of the occupation numbers in time, if the overlap of the initial state and a tunneling pair is strong [21, 27] (see Fig.14.17, right plot).

Suppose we have a large lattice, and put initially many quanta on one site. Then any tunneling of this packet as a whole will occur on very long time scales. On time scales much shorter, we may describe the excitation as a classical discrete breather state plus a small perturbation. Treating that perturbation quantum mechanically, one could expect that the time-periodic DB acts as a constant source of quantum radiation for the quantized phonon field. It turns out to be impossible, for very much the same reasons as in the purely classical treatment (see [30]). This result implies, that there is almost no other source of decay for a localized initial state in a quantum lattice, but to slowly tunnel as a whole along the lattice, if nonlinearities allow for the formation of exact classical DB states [31]. Numerical calculations for such a case, but with few quanta, were performed by Proville [32], and, similar to the above trimer discussion, showed that if quantum breather states exist in the system, then localized excitations stay localized for times which are much longer than the typical phonon diffusion times in the absence of anharmonicity.

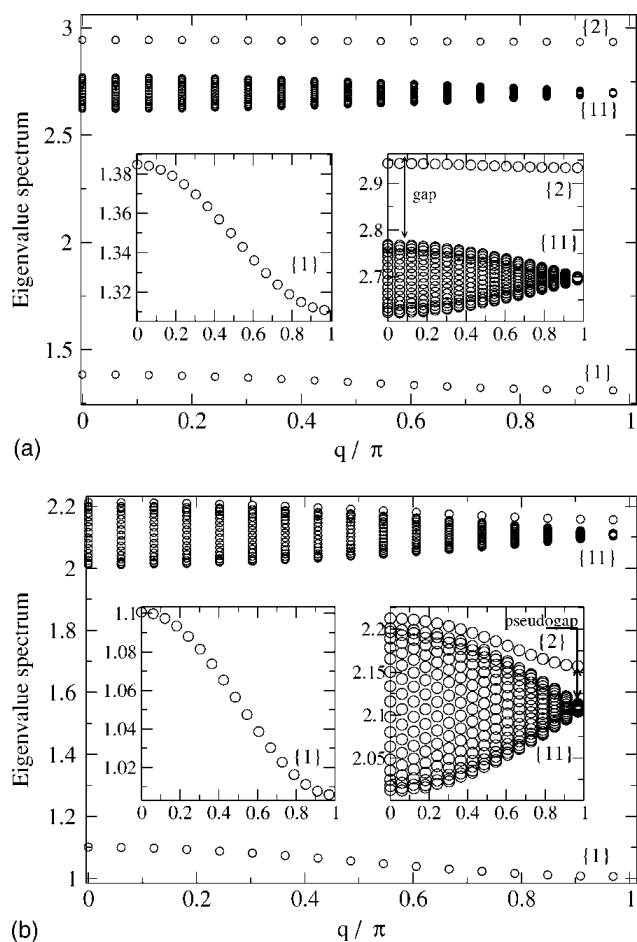


Figure 14.14: Eigenspectrum of a chain with 33 sites for parameters (a) $C = 0.05$, $v_4 = 0.2$, and (b) $C = 0.05$, $v_4 = 0.02$. The inserts show magnifications of the fundamental branch (left) and overtone region (right). The quantum breather branch is marked by (2), and the two-phonon band by (11). Adapted from [23].

14.3.2 Splitting and correlations

QBs are nearly degenerate eigenstates. For the dimer and the trimer, they come in symmetric-antisymmetric pairs. So one may compute the nearest neighbor energy spacing (tunneling splitting) between pairs of symmetric-antisymmetric eigenstates in order to identify QBs. Since QBs correspond to classical orbits that are characterized by energy localization, they may be identified by defining correlation functions. For large lattices it has been shown that QBs have exponentially localized correlation functions, in full analogy to their classical counterparts.

For the dimer and the trimer, the correlation functions may be defined as follows:

$$f_\mu(1,2) = \langle \hat{n}_1 \hat{n}_2 \rangle_\mu, \quad f_\mu(1,1) = \langle \hat{n}_1^2 \rangle_\mu, \quad (14.27)$$

where $\hat{n}_i = \hat{a}_i^\dagger \hat{a}_i$, and $\langle \hat{A} \rangle_\mu = \langle \chi_\mu | \hat{A} | \chi_\mu \rangle$, $\{|\chi_\mu\rangle\}$ being the set of eigenstates of the system. The ratio $0 \leq f_\mu(1,2)/f_\mu(1,1) \leq 1$ measures the site correlation of quanta: it is small when

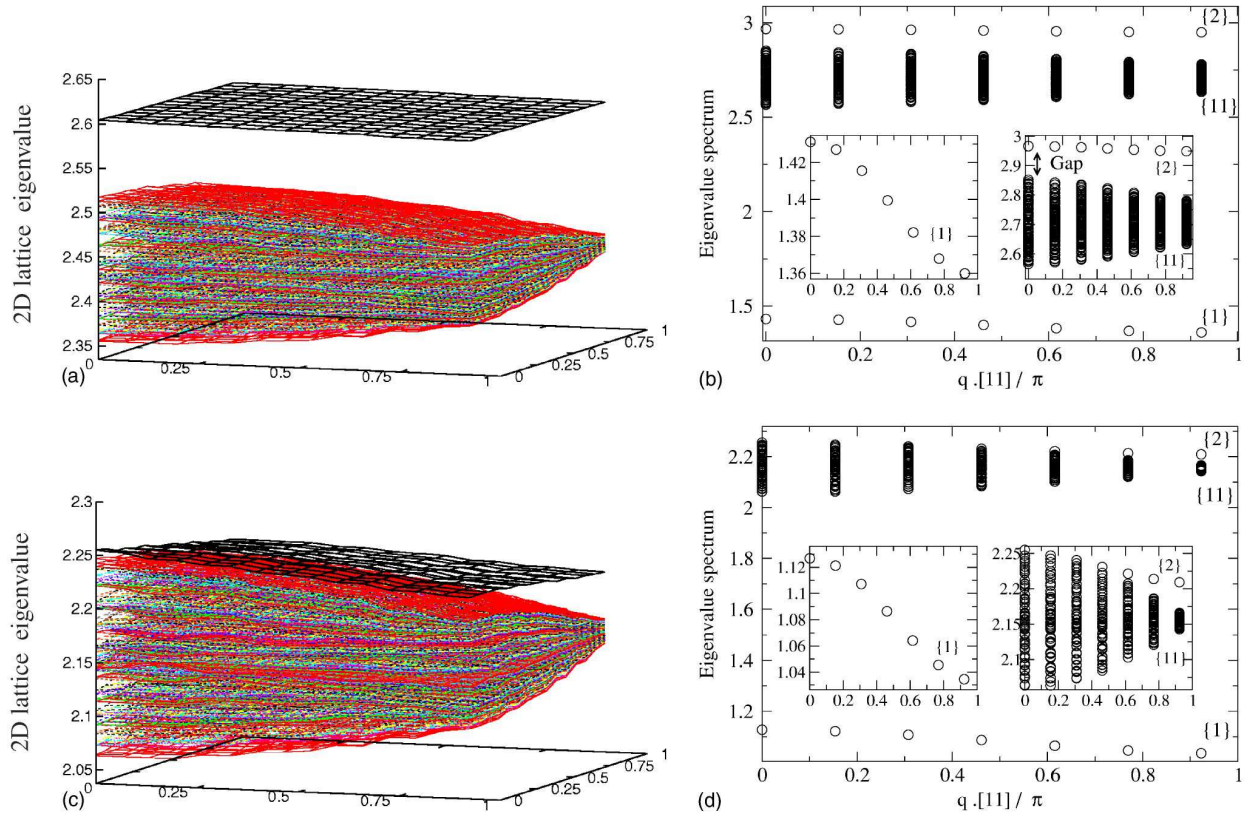


Figure 14.15: Eigenspectrum of a lattice with 13×13 sites for parameters (top) $C = 0.025$, $v_4 = 0.1$, and (bottom) $C = 0.025$, $v_4 = 0.025$. Left plots - spectra over the whole Brillouin zone. Right plots - profiles of the spectra along the direction $[11]$. The insets show the magnifications of the phonon branch (left) and the quantum breather energy region (right). Adapted from [23].

quanta are site-correlated (i.e. when many quanta are located on one site there are almost none on the other one) and close to unity otherwise.

For the dimer case, the relation $b = n_1 + n_2$, leads to

$$f_\mu(1, 2) = b \langle \hat{n}_1 \rangle_\mu - \langle \hat{n}_1^2 \rangle_\mu. \quad (14.28)$$

In Fig. 14.18-left we show the energy splitting and the correlation function of the eigenstates. We see that beyond a threshold (dashed line), the splitting drops exponentially fast with energy. The corresponding pairs of eigenstates, which are tunneling pairs, are site correlated. Thus they are QBs. Their correlation functions show a fast decrease for energies above the threshold. In these states many quanta are localized on one site of the dimer and the tunneling time of such an excitation from one site to the other (given by the inverse energy splitting between the eigenstates of the pair) is exponentially large. As shown in Ref. [17], this energy threshold is close to the threshold for the existence of DBs in the corresponding classical model.

QBs are close to symmetric (S) and antisymmetric (A) eigenstates of the $C = 0$ case

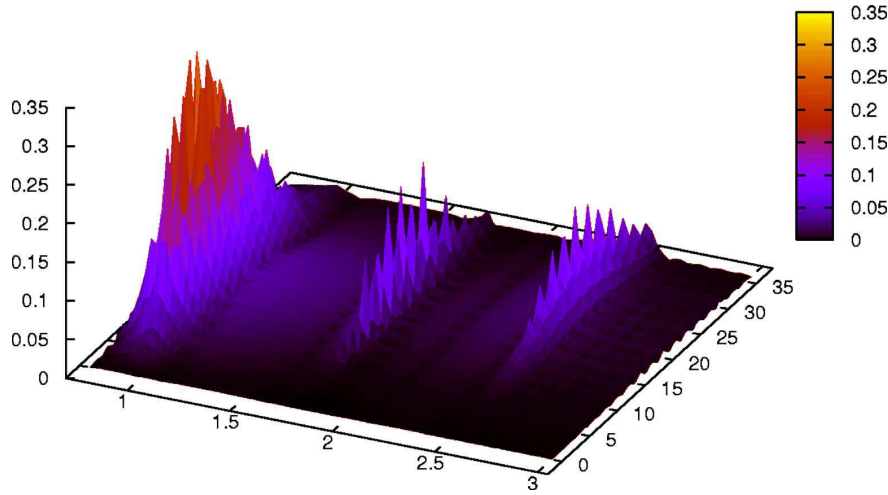


Figure 14.16: A 3D plot of the inelastic structure factor $S(q, \omega)$ as a function of the dimensionless energy transfer $0 \leq \omega \leq 3$ and the scalar product of the transfer momentum \mathbf{q} and the polarization \mathbf{u} . Adapted from [24].

given by

$$|n_1, n_2\rangle_{S,A} = \frac{1}{\sqrt{2}}(|n_1, n_2\rangle \pm |n_2, n_1\rangle), \quad (14.29)$$

with $n_{1,2} \gg n_{2,1}$. So we may estimate the dependence of the correlation functions on n_1 using the eigenstates (14.29) and $b = n_1 + n_2$. The result is:

$$\frac{f(1, 2)_{n_1}}{f(1, 1)_{n_1}} = \frac{2n_1(b - n_1)}{n_1^2 + (b - n_1)^2}, \quad (14.30)$$

where we note that it is equal to unity when $n_1 = b/2$, and vanishes when $n_1 = 0, b$.

Using the relation between the eigenenergy ε of the $C = 0$ case and the number n_1 ($= 1, 2, \dots, b$)

$$\varepsilon_{n_1} = \frac{5}{4} + \frac{3}{2}b + \frac{1}{2} [n_1^2 + (b - n_1)^2], \quad (14.31)$$

one may obtain the energy dependence of the correlation function (14.30), which is plotted in Fig. 14.18-b (thin solid line). We can see that beyond the energy threshold for appearance of QBs, the numerical results are close to the estimation (14.30).

14.3.3 Entanglement

QBs may also be differentiated from other quantum states when measuring the degree of entanglement [33, 34]. For the dimer and the trimer the degree of entanglement in the eigenstates may be measured by minimizing the distance of a given state to the space of product states of the dimer part (expanded by the product basis $\{|n_1\rangle \otimes |n_2\rangle\}$), which

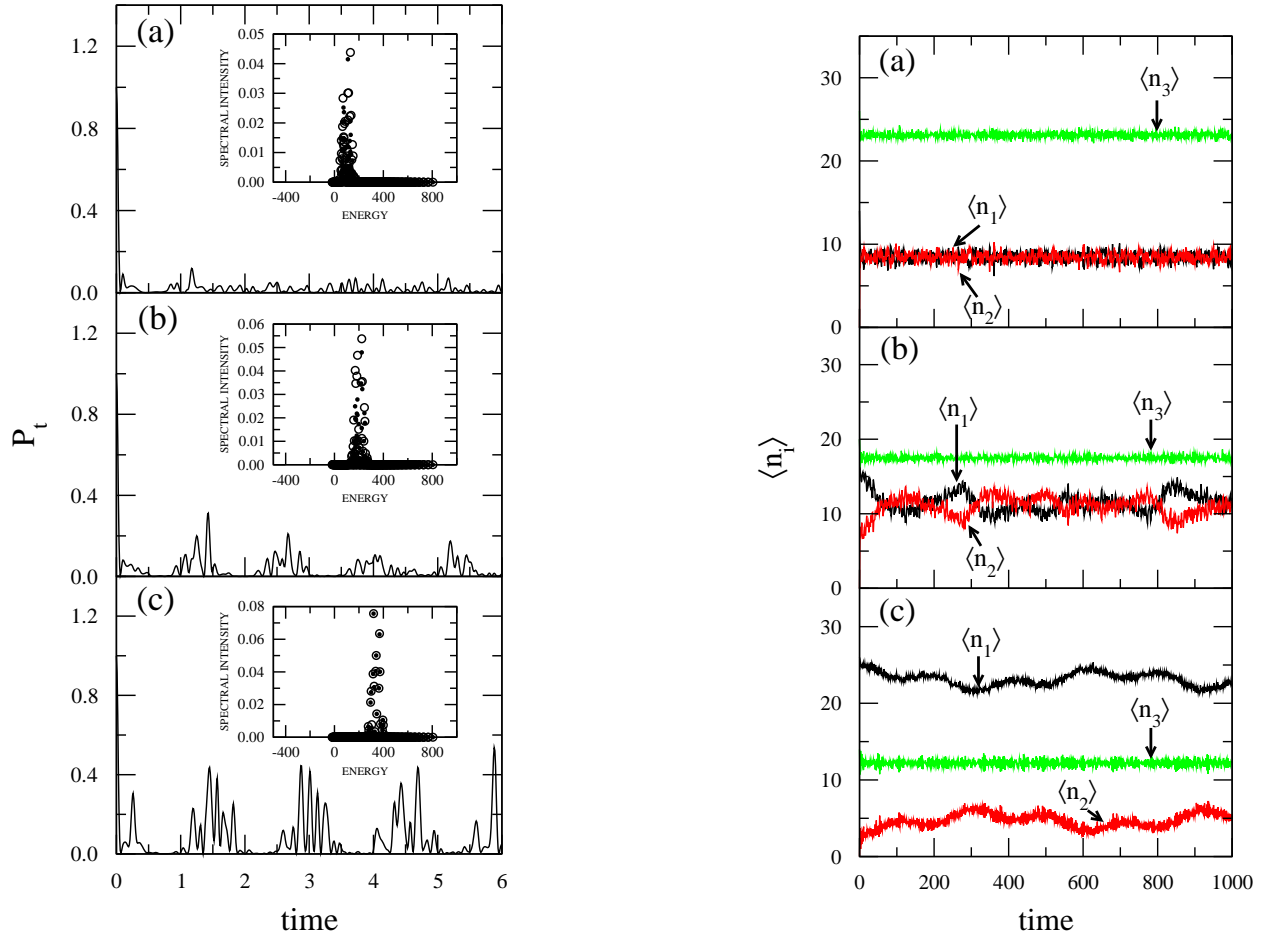


Figure 14.17: Left plot: Survival probability of the initial state $|\Psi_0\rangle = |20 + \nu, 0, 20 - \nu\rangle$. $\nu =$ (a) -6, (b) 0, and (c) 6. Insets: spectral intensity of the initial state $|\Psi_0\rangle$. Filled circles - symmetric eigenstates; open circles - antisymmetric eigenstates. Right plot: Time evolution of expectation values of the number of bosons at each site of the trimer for different initial states $|\Psi_0\rangle = |20 + \nu, 0, 20 - \nu\rangle$. $\nu =$ (a) -6, (b) 0, and (c) 6. Adapted from [21].

depends on the largest eigenvalue of the corresponding reduced density matrix [29, 35–37]:

$$\Delta = \sum_{n_1, n_2}^N (\chi_{n_1, n_2} - f_{n_1} g_{n_2})^2, \quad (14.32)$$

where for the case of the dimer $\chi_{n_1, n_2} = \langle n_1, n_2 | \chi \rangle$, and for the trimer $\chi_{n_1, n_2} = \langle n_1, n_2, (n_3 = b - n_1 - n_2) | \chi \rangle$. The functions f_{n_1} and g_{n_2} are such that Δ is minimum [29]. Δ measures how far a given eigenstate of the system is from being a product of single-site states, and has values $0 < \Delta < 1$. This measure has a direct relation to the distance of a given eigenstate from a possible one obtained after performing a Hartree approximation [35].

For the dimer, since QB states are close to eigenstates of the $C = 0$ case

$$|\chi\rangle_{QB} \simeq \frac{1}{\sqrt{2}}(|n, 0\rangle \pm |0, n\rangle), \quad (14.33)$$

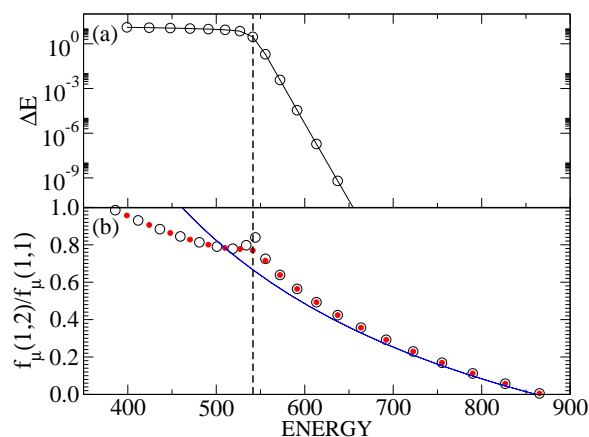


Figure 14.18: (a) Energy splitting and (b) correlation function vs. energy of the eigenstates of the dimer (open circles, symmetric eigenstates; solid circles, antisymmetric eigenstates). The vertical dashed line marks the energy threshold for appearance of QB states. The thin solid line in (a) is a guide for the eye, whereas in (b) it is the estimation using eq. (14.30). Here $b = 40$ and $C = 2$.

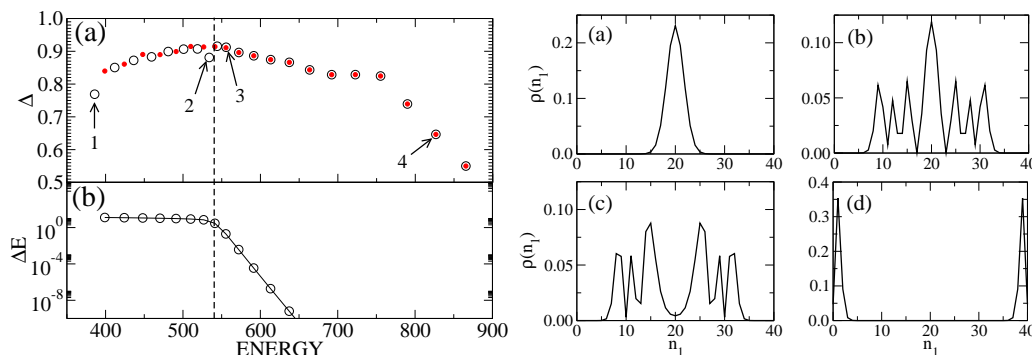


Figure 14.19: Left panel: (a) Entanglement of the eigenstates and (b) energy splitting as a function of energy in the dimer (open circles, symmetric eigenstates; solid circles, antisymmetric eigenstates). The vertical dashed line marks the energy threshold for appearance of QB states. Here $b = 40$, and $C = 2$. Right panel: The density of the symmetric eigenstates marked by labeled arrows in left panel-a: (a) S-0 (arrow 1), (b) S-7 (arrow 2), (c) S-9 (arrow 3), (d) S-19 (arrow 4).

with $n \lesssim b$, one expects that the degree of entanglement in QB states is similar to the degree of entanglement in such states. Since only two basis states are involved, it can not be a state of maximum entanglement. For $C = 0$ the eigenstates of the system are the basis states given by eq. (14.29), where for $n_1 = n_2$ it follows that $\Delta = 0$, and for $n_1 \neq n_2$ (which includes the state in eq. 14.33) $\Delta = 0.5$.

In previous works in a similar quantum dimer model [33, 34], it was shown that at the energy threshold for appearance of QB states the entanglement (in this case measured in a different way) becomes maximum and then decreases with energy. From this, and the above reasoning, we expect that QB states show decreasing entanglement Δ with energy, tending

to 0.5. Results in left panel-a of Fig. 14.19 agree with this expectation.

For $C = 0$, the entanglement has the values 0 and 0.5 corresponding to the basis states $|b/2, b/2\rangle$ and $|n, b - n\rangle$ ($n \neq b/2$) with equal and distinct number of quanta at each site respectively. When $C > 0$, the eigenstates become linear superpositions of the basis states and the entanglement rises, being larger as long as more basis states are involved in building up an eigenstate. This can be seen in the right panel of Fig. 14.19, where we plot the density $\rho(n_1, n_2 = b - n_1) = |\langle n_1, b - n_1 | \chi \rangle|^2 \equiv \rho(n_1)$ of four symmetric eigenstates marked by labeled arrows in the left panel: The low-energy eigenstate marked by the arrow 1 consists mainly of one basis state: $|b/2, b/2\rangle$, as seen in the right panel-a, hence the entanglement is relatively small. When going up in energy the entanglement in the eigenstates quickly increases, becoming maximum at the energy threshold, and then decreases. An eigenstate just before the threshold like the one marked by the arrow 2 in the left panel involves many basis states fulfilling $n_1 + n_2 = b = 40$ (right panel-b), hence the entanglement is large. However, for a QB state lying in the energy region beyond the threshold, like the one marked by the arrow 3 in the left panel, the number of involved basis states, and thus the entanglement starts to decrease (right panel-c). Finally, in high-energy eigenstates like the one marked by the arrow 4 in the left panel, which has the form shown in eq. (14.33) (right panel-d), the entanglement is even smaller and gets close to 0.5 as expected.

From the above results we see that by measuring entanglement one may gain information not only about the energy threshold for existence of QBs (also visible when measuring the energy splitting and correlation function), but also about how many basis states overlap strongly with the eigenstate under consideration. We also computed the *von Neumann entropy* [38], which is another standard measure of entanglement, and the results were consistent with those discussed above.

14.4 Quantum edge-localized states

Most of the studies about QBs in large lattices (with few bosons) were done considering a system with periodic boundary conditions, and thus, translational invariant. However, usually real systems have to be modeled with open boundary conditions. Hence it is natural to wonder what happens with QBs when the lattice has finite size, and therefore, no translational invariance.

In the classical case, it has been shown that in finite nonlinear lattices, the breaking of the translational symmetry may lead to the formation of so called *nonlinear edge states*. These are excitations which are localized at the edges of the lattice and they have been studied, in particular, in nonlinear optics experiments employing optical waveguides, being coined with the name of *discrete surface solitons* [39]. In particular, it is well known that the discrete nonlinear Schrödinger equation (DNLS) has time-periodic solutions localized at the edge of the lattice [40, 41]. It is therefore expected that the large-boson limit of the open-boundary Bose-Hubbard model will show eigenstates in which the bosons are localized at the edge.

Numerical studies by Pouthier were done to answer the edge-localization question in a lattice with a few bosons [42], where the mean-field approximation (DNLS equation) cannot *a priori* be expected to provide the correct intuition. The answer turns out to be subtle — this phenomenon is not present for the case of two particles, but appears when the particle number is three or more [42]. Further studies focused on the energy spectrum and eigenstates

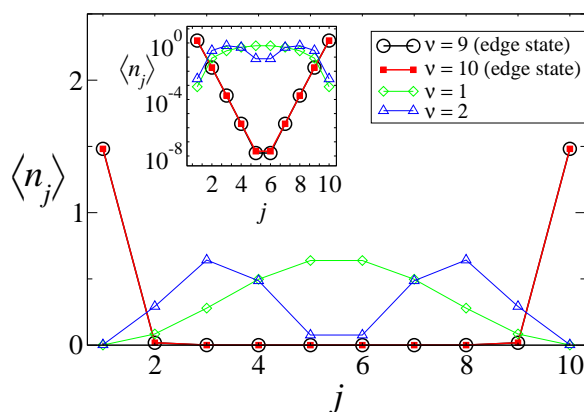


Figure 14.20: Spatial profile of site occupancies for several eigenstates of the three-boson Bose-Hubbard chain. The index ν counts the eigenstates from the lowest-energy one ($\nu = 1$). Inset shows the same plot in semilog scale, the linear behavior indicating exponential localization in the edge states. This image was taken from Ref. [43]

(Fig. 14.20) were done by Pinto *et al* [43], where degenerate perturbation theory allowed to explain why edge-localized states exist only if the number of particles is three or more [43].

14.5 Quantum breathers with fermions

Advances in experimental techniques of manipulation of ultracold atoms in optical lattices make it feasible to explore the physics of few-body interactions. Systems with few quantum particles on lattices have new unexpected features as compared to the condensed matter case of many-body interactions, where excitation energies are typically small compared to the Fermi energy. Therefore it is of interest to study binding properties of fermionic pairs with total spin zero, as recently presented in Ref. [44]. We use the extended Hubbard model, which contains two interaction scales - the on site interaction U and the nearest neighbour intersite interaction V . The nonlocal interaction V is added in condensed matter physics to emulate remnants of the Coulomb interaction due to non-perfect screening of electronic charges. For fermionic ultracold atoms or molecules with magnetic or electric dipole-dipole interactions, it can be tuned with respect to the local interaction U by modifying the trap geometry of a condensate, additional external dc electric fields, combinations with fast rotating external fields, etc (for a review and relevant references see [45]).

Consider a one-dimensional lattice with f sites and periodic boundary conditions described by the extended Hubbard model with the following Hamiltonian:

$$\hat{H} = \hat{H}_0 + \hat{H}_U + \hat{H}_V, \quad (14.34)$$

where

$$\hat{H}_0 = - \sum_{j,\sigma} \hat{a}_{j,\sigma}^+ (\hat{a}_{j-1,\sigma} + \hat{a}_{j+1,\sigma}), \quad (14.35)$$

$$\hat{H}_U = -U \sum_j \hat{n}_{j,\uparrow} \hat{n}_{j,\downarrow}, \quad \hat{n}_{j,\sigma} = \hat{a}_{j,\sigma}^+ \hat{a}_{j,\sigma}, \quad (14.36)$$

$$\hat{H}_V = -V \sum_j \hat{n}_j \hat{n}_{j+1}, \quad \hat{n}_j = \hat{n}_{j,\uparrow} + \hat{n}_{j,\downarrow}. \quad (14.37)$$

\hat{H}_0 describes the nearest-neighbor hopping of fermions along the lattice. Here the symbols $\sigma = \uparrow, \downarrow$ stand for a fermion with spin up or down. \hat{H}_U describes the onsite interaction between the particles, and \hat{H}_V the intersite interaction of fermions located at adjacent sites. $\hat{a}_{j,\sigma}^+$ and $\hat{a}_{j,\sigma}$ are the fermionic creation and annihilation operators satisfying the corresponding anticommutation relations: $\{\hat{a}_{j,\sigma}^+, \hat{a}_{l,\sigma'}\} = \delta_{j,l} \delta_{\sigma,\sigma'}$, $\{\hat{a}_{j,\sigma}^+, \hat{a}_{l,\sigma'}^+\} = \{\hat{a}_{j,\sigma}, \hat{a}_{l,\sigma'}\} = 0$. Note that throughout this work we consider U and V positive, which leads to bound states located below the two-particle continuum. A change of the sign of U, V will simply swap the energies.

To observe the fermionic character of the considered states, any two-particle number state is generated from the vacuum $|O\rangle$ by first creating a particle with spin down, and then a particle with spin up: e.g. $\hat{a}_{2,\uparrow}^+ \hat{a}_{1,\downarrow}^+ |O\rangle$ creates a particle with spin down on site 1 and one with spin up on site 2, while $\hat{a}_{2,\uparrow}^+ \hat{a}_{2,\downarrow}^+ |O\rangle$ creates both particles with spin down and up on site 2.

Due to periodic boundary conditions the Hamiltonian (14.34) commutes also with the translation operator \hat{T} , which shifts all lattice indices by one. It has eigenvalues $\tau = \exp(ik)$, with Bloch wave number $k = \frac{2\pi\nu}{f}$ and $\nu = 0, 1, 2, \dots, f-1$.

For the case of having only one fermion (either spin up or spin down) in the lattice ($n = 1$), a number state has the form $|j\rangle = \hat{a}_{j,\sigma}^+ |O\rangle$. The interaction terms \hat{H}_U and \hat{H}_V do not contribute. For a given wave number k , the eigenstate to (14.34) is therefore given by:

$$|\Psi_1\rangle = \frac{1}{\sqrt{f}} \sum_{s=1}^f \left(\frac{\hat{T}}{\tau}\right)^{s-1} |1\rangle. \quad (14.38)$$

The corresponding eigenenergy

$$\varepsilon_k = -2 \cos(k). \quad (14.39)$$

For two particles, the number state method involves $N_s = f^2$ basis states, which is the number of ways one can distribute two fermions with opposite spins over the f sites including possible double occupancy of a site. Below we consider only cases of odd f for simplicity. Extension to even values of f is straightforward. The details of the calculations can be found in [44].

In Fig. 14.21 we show the energy spectrum of the Hamiltonian matrix obtained by numerical diagonalization for the interaction parameters $U = 2$ and $V = 2$ and $f = 101$. At $U = 0$ and $V = 0$, the spectrum is given by the two fermion continuum, whose eigenstates are characterized by the two fermions independently moving along the lattice. In this case the eigenenergies are the sum of the two single-particle energies:

$$E_{k_1, k_2}^0 = -2[\cos(k_1) + \cos(k_2)], \quad (14.40)$$

with $k_{1,2} = \pi\nu_{1,2}/(f+1)$, $\nu_{1,2} = 1, \dots, f$. The Bloch wave number $k = k_1 + k_2 \bmod 2\pi$. Therefore, if $k = \pm\pi$, the continuum degenerates into points. The continuum is bounded by the hull curves $h_{\pm}(k) = \pm 4 \cos \frac{k}{2}$. The same two-particle continuum is still observed in Fig.

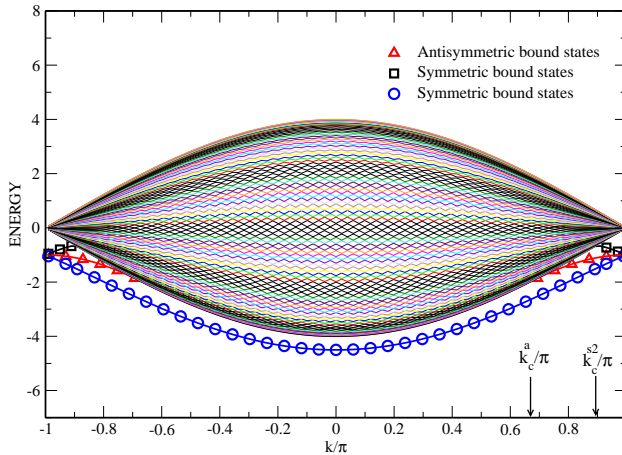


Figure 14.21: (Color online) Energy spectrum of the two fermion states. The eigenvalues are plotted as a function of the wave number k . Here $U = 1$, $V = 1$, $f = 101$. Symbols are from analytical derivation, lines are the result of numerical diagonalization. The arrows indicate the location of the critical wave numbers (see text). Adapted from [44].

14.21 for nonzero interaction. However, in addition to the continuum, we observe one, two or three bound states dropping out of the continuum, which depends on the wave number. For any nonzero U and V , all three bound states drop out of the continuum at $k = \pm\pi$. One of them stays bounded for all values of k . The two other ones merge with the continuum at some critical value of $|k|$ upon approaching $k = 0$ as observed in Fig.14.21. Note that for $k = \pm\pi$ and $U = V$, all three bound states are degenerate.

Upon increasing U and V , we observe that a second bound state band separates from the continuum for all k (Fig.14.22). At the same time, when $U \neq V$, the degeneracy at $k = \pm\pi$ is reduced to two.

Finally, for even larger values of U and V , all three bound state bands completely separate from the continuum (Fig.14.23).

14.5.1 Symmetric and antisymmetric state representation

In order to obtain analytical estimates on the properties of the observed bound states, we use the fact that the Hamiltonian for a two fermion state is invariant under flipping the spins of both particles. We define symmetric basis states

$$|\Phi_{j,s}\rangle = \frac{1}{\sqrt{2}}(|\Phi_{j,+}\rangle + |\Phi_{j,-}\rangle) \quad (14.41)$$

and antisymmetric states

$$|\Phi_{j,a}\rangle = \frac{1}{\sqrt{2}}(|\Phi_{j,+}\rangle - |\Phi_{j,-}\rangle). \quad (14.42)$$

Note that $|\Phi_1\rangle$ is a symmetric state as well.

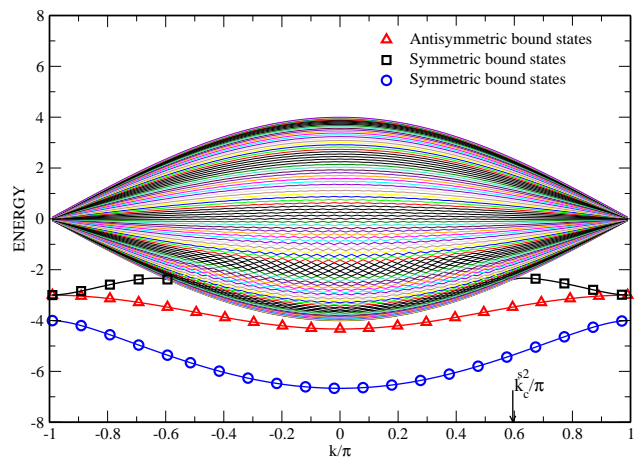


Figure 14.22: (Color online) Energy spectrum of the two fermion states. The eigenvalues are plotted as a function of the wave number k . Here $U = 4$, $V = 3$, $f = 101$. The symbols are from analytical derivation, lines are the results of numerical diagonalization. The arrow indicates the location of the critical wave number (see text). Adapted from [44].

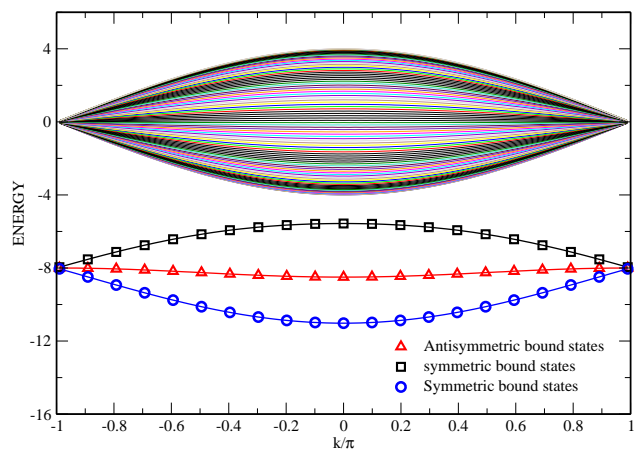


Figure 14.23: (Color online) Energy spectrum for the two fermion states. The eigenvalues are plotted as a function of the wave number k . Here $U = 8$, $V = 8$, $f = 101$. The symbols are from analytical derivation, lines are the results of numerical diagonalization. Adapted from [44].

14.5.2 Antisymmetric bound states

The antisymmetric states exclude double occupation. Therefore the spectrum is identical with the one of two spinless fermions [13]. Following the derivations in [13] we find that the antisymmetric bound state, if it exists, has an energy

$$E_2^a(k) = -(V + \frac{4}{V} \cos^2(\frac{k}{2})) . \quad (14.43)$$

This result is valid as long as the bound state energy stays outside of the continuum. The critical value of k at which validity is lost, is obtained by requesting $|E_2^a(k)| = |h_{\pm}(k)|$. It follows $V = 2 \cos(\frac{k}{2})$. Therefore the antisymmetric bound state merges with the continuum at a critical wave number

$$k_c^a = 2 \arccos(\frac{V}{2}) , \quad (14.44)$$

setting a critical length scale $\lambda_c^a = \frac{2\pi}{k_c^a}$. For $V = 1$ it follows $k_c^a/\pi \approx 0.667$ (see Fig.14.21).

The equation (14.43) is in excellent agreement with the numerical data in Figs. 14.21,14.22,14.23 (cf. open triangles). We also note, that the antisymmetric bound state is located between the two symmetric bound states, which we discuss next.

14.5.3 Symmetric bound states

A bound state can be searched for by assuming an unnormalized eigenvector of the form $|c, 1, \mu, \mu^2, \mu^3, \dots\rangle$ with $|\mu| \equiv \rho \leq 1$. We obtain [44]

$$E_2^s(k) = -2(\rho + \frac{1}{\rho}) \cos k/2 . \quad (14.45)$$

The parameter ρ satisfies a cubic equation

$$a\rho^3 + b\rho^2 + c\rho + d = 0 \quad (14.46)$$

with the real coefficients a, b, c and d given by $a = 2V \cos(\frac{k}{2})$, $b = 4\cos^2(\frac{k}{2}) - UV$, $c = 2(U + V)\cos(\frac{k}{2})$, $d = -4\cos^2(\frac{k}{2})$. We plot the results in Figs. 14.21,14.22,14.23 (cf. open circles and squares). We obtain excellent agreement.

At the Brillouin zone edge $k = \pm\pi$ the cubic equation (14.46) is reduced to a quadratic one, and can be solved to obtain finally $\rho \rightarrow 0$ and

$$E_2^{s1}(k \rightarrow \pm\pi) = -U , \quad E_2^{s2}(k \rightarrow \pm\pi) = -V . \quad (14.47)$$

In particular we find for $k = \pm\pi$ that $E_2^{s2} = E_2^a$. In addition, if $U = V$, all three bound states degenerate at the zone edge.

If $V = 0$, the cubic equation (14.46) is reduced to a quadratic one in the whole range of k and yields [13]

$$E_2^{s1}(k) = -\sqrt{U^2 + 16 \cos^2(k/2)} . \quad (14.48)$$

Next we determine the critical value of k for which the bound state with energy E_2^{s2} is joining the continuum. Since at this point $\rho = 1$, we solve (14.46) with respect to k_c and find

$$k_c^{s2} = 2 \arccos \left(\frac{UV}{2(U+2V)} \right) \quad (14.49)$$

setting another critical length scale $\lambda_c^s = \frac{2\pi}{k_c^s}$. E.g. for $U = V = 1$ $k_c^{s2}/\pi \approx 0.89$, in excellent agreement with Fig.14.21. For $U = 4$ and $V = 3$ we find $k_c^{s2}/\pi \approx 0.59$ confirming numerical results in Fig.14.22.

14.6 Small Josephson junction networks

Recent studies of Pinto et al [28, 29] deal with quantum breather excitations in two capacitively coupled Josephson junctions. Such systems are currently under experimental investigation, being candidates for quantum information processing, and show remarkably long coherence times up to 100 ns for few quanta excitations. The system does not conserve the number of excited quanta, and can be best compared with the above Bose-Hubbard trimer. Quantum breather signatures are found simultaneously in the spectra (tunneling splittings), correlation functions, entanglement, and quanta number fluctuations.

We address the excitation of QBs in a system of two coupled Josephson junctions in the quantum regime [29]. Josephson junctions are nonlinear devices that show macroscopic quantum behavior, and nowadays they can be manipulated with high precision, in such a way that the energy flow between coupled junctions can be resolved in time.

Josephson junctions behave like anharmonic oscillators, and by lowering the temperature one can bring them into the quantum regime, where their quantization leads to energy levels which are nonequidistant because of the anharmonicity. These levels can be separately excited by using microwave pulses, and the energy distribution between the junctions can be measured in time using subsequent pulses [46]. So far these techniques have been used for experiments on quantum information processing with Josephson junctions [47–49], but we think that arrays of Josephson junctions in the quantum regime also might be used as playgrounds for experiments on quantum dynamics of excitations in nonlinear lattices.

The system is sketched in Fig.14.24-a: two JJs are coupled by a capacitance C_c , and they are biased by the same current I_b . The strength of the coupling due to the capacitor is $\zeta = C_c/(C_c + C_J)$. The dynamics of a biased Josephson junction (JJ) is analogous to the dynamics of a particle with a mass proportional to the junction capacitance C_J , moving on a tilted washboard potential

$$U(\varphi) = -I_c \frac{\Phi_0}{2\pi} \cos \varphi - I_b \varphi \frac{\Phi_0}{2\pi}, \quad (14.50)$$

which is sketched in Fig.14.24-b. Here φ is the phase difference between the macroscopic wave functions in both superconducting electrodes of the junction, I_b is the bias current, I_c is the critical current of the junction, and $\Phi_0 = h/2e$ the flux quantum. When the energy of the particle is large enough to overcome the barrier ΔU (that depends on the bias current I_b) it escapes and moves down the potential, switching the junction into a resistive state with a nonzero voltage proportional to $\dot{\varphi}$ across it. Quantization of the system leads

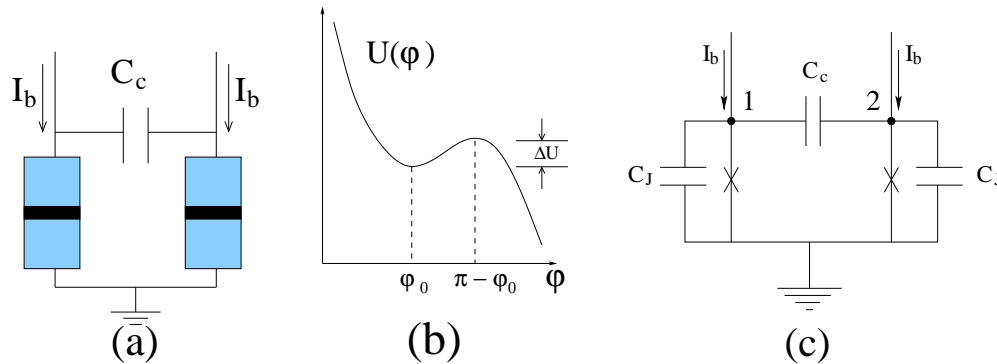


Figure 14.24: (a) Sketch of the two capacitively coupled Josephson junctions. (b) Sketch of the washboard potential for a single current-biased Josephson-junction. (c) Circuit diagram for two ideal capacitively coupled Josephson junctions.

to discrete energy levels inside the potential wells, which are nonequidistant because of the anharmonicity. Note that even if there is not enough energy to classically overcome the barrier, the particle may perform a quantum escape and tunnel outside the well, thus switching the junction into the resistive state. Thus each state inside the well is characterized by a bias and state-dependent lifetime, or its inverse —the escape rate.

The Hamiltonian of the system is

$$H = \frac{P_1^2}{2m} + \frac{P_2^2}{2m} + U(\varphi_1) + U(\varphi_2) + \frac{\zeta}{m} P_1 P_2, \quad (14.51)$$

where

$$m = C_J(1 + \zeta) \left(\frac{\Phi_0}{2\pi} \right)^2, \quad (14.52)$$

$$P_{1,2} = (C_c + C_J) \left(\frac{\Phi_0}{2\pi} \right)^2 (\dot{\varphi}_{1,2} - \zeta \dot{\varphi}_{2,1}). \quad (14.53)$$

Note that the conjugate momenta $P_{1,2}$ are proportional to the charge at the nodes of the circuit (which are labeled in Fig.14.24-c).

In the quantum case the energy eigenvalues and the eigenstates of the system were computed and analyzed in [29]. In Fig.14.25 we show the nearest neighbor energy spacing (tunneling splitting) and the correlation function of the eigenstates. For this, and all the rest, we used $I_c = 13.3 \mu\text{A}$, $C_J = 4.3 \text{ pF}$, and $\zeta = 0.1$, which are typical values in experiments. We see that in the central part of the spectrum the energy splitting becomes small in comparison to the average. The corresponding pairs of eigenstates, which are tunneling pairs, are site correlated, and thus QBs. In these states many quanta are localized on one junction and the tunneling time of such an excitation from one junction to the other (given by the inverse energy splitting between the eigenstates of the pair) can be exponentially large and depend sensitively on the number of quanta excited.

Note that the tunneling of quanta between the JJs occurs without an obvious potential energy barrier being present (the interaction between the junctions is only through their

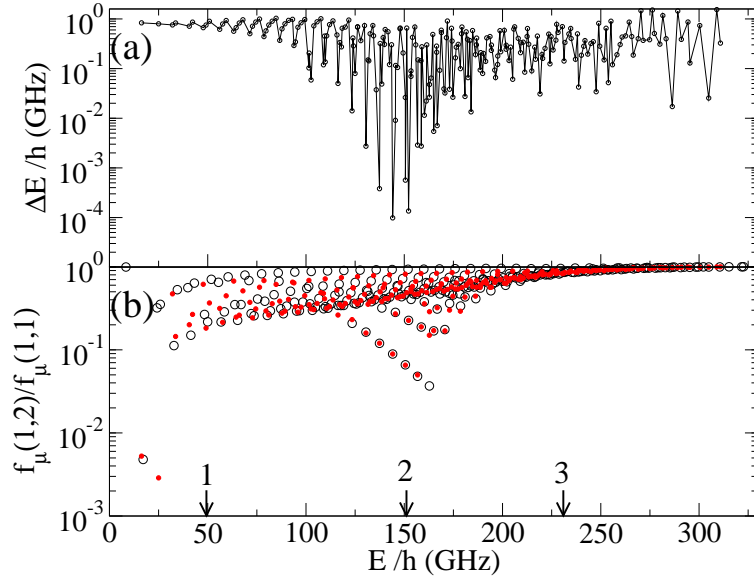


Figure 14.25: (a) Energy splitting and (b) correlation function vs. energy of the eigenstates of the two-junctions system (open circles, symmetric eigenstates; filled circles, antisymmetric eigenstates). The labeled arrows mark the energy corresponding to the peak of the spectral intensity in Fig.14.26-b, d, and f (see text). The parameters are $\gamma = Ib/Ic = 0.945$ and $\zeta = 0.1$ (22 levels per junction).

momenta). This process has been coined *dynamical tunneling* [50–52], to distinguish from the usual tunneling through a potential barrier. In dynamical tunneling, the barrier—a so-called invariant separatrix manifold—is only visible in phase space, where it separates two regions of regular classical motion between which the tunneling process takes place. Therefore, when referring to the tunneling between the JJs, we implicitly mean that it is dynamical.

The fact that the strongest site correlated eigenstates occur in the central part of the energy spectrum may be easily explained as follows: Let N be the highest excited state in a single junction, with a corresponding maximum energy ΔU (Fig.14.24). For two junctions the energy of the system with both junctions in the N -th state is $2\Delta U$, which roughly is the width of the full spectrum. Thus states of the form $|N, 0\rangle$ and $|0, N\rangle$ that have energy ΔU are located approximately in the middle.

Having the eigenvalues and eigenstates, we compute the time evolution of different initially localized excitations, and the expectation value of the number of quanta at each junction $\langle \hat{n}_i \rangle(t) = \langle \Psi(t) | \hat{n}_i | \Psi(t) \rangle$. Results are shown in Fig.14.26a, c, and e. We also compute the spectral intensity $I_\mu^0 = |\langle \chi_\mu | \Psi_0 \rangle|^2$, which measures the strength of overlap of the initial state $|\Psi_0\rangle$ with the eigenstates. Results are shown in Fig.14.26-b, d, and f, where we can see a peak in each case, which corresponds to the arrows in Fig.14.25-b. We can see that the initial state $|\Psi_0\rangle = |0, 5\rangle$ overlaps with eigenstates with an energy splitting between them being relatively large and hence the tunneling time of the initially localized excitation is short. For the case $|\Psi_0\rangle = |0, 19\rangle$ QBs are excited: The excitation overlaps strongly with tunneling pairs of eigenstates in the central part of the spectrum, which are site correlated and nearly degenerate. The tunneling time of such an excitation is very long, and thus keeps the quanta localized on their initial excitation site for corresponding times. Finally

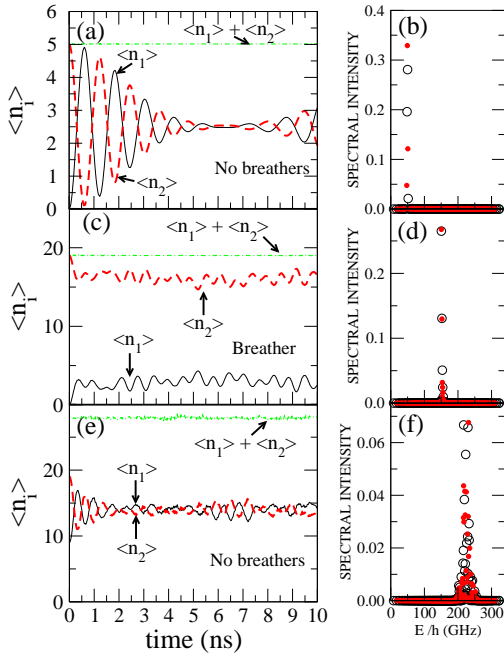


Figure 14.26: Time evolution of expectation values of the number of quanta at each junction (left panels) for different initial excitations with corresponding spectral intensities (right panels). (a) and (b): $|\Psi_0\rangle = |0, 5\rangle$; (c) and (d): $|\Psi_0\rangle = |0, 19\rangle$; (e) and (f): $|\Psi_0\rangle = |9, 19\rangle$. Open circles, symmetric eigenstates; filled circles, antisymmetric eigenstates. The energies of the peaks in the spectral intensity are marked by labeled arrows in Fig.14.25-b (see text). The parameters are $\gamma = Ib/Ic = 0.945$ and $\zeta = 0.1$ (22 levels per junction).

the initial state $|\Psi_0\rangle = |9, 19\rangle$ overlaps with weakly site correlated eigenstates with large energy splitting. Hence the tunneling time is short again.

We computed also the time evolution of the expectation values of the number of quanta for initial conditions which are coherent or incoherent (mixtures) superpositions of product basis states with equal weights. This is relevant for experiments, since it may be hard to excite one junction to a determined state but easier to excite several states of the junction at the same time. We used coherent superpositions (characterized by well defined states $|\Psi_0\rangle$), and mixtures (characterized by their corresponding density operators $\hat{\rho}_0$), of four basis states around the already used initial states: For the state $|0, 5\rangle$ we superposed the basis states $|0, 5\rangle$, $|0, 6\rangle$, $|0, 7\rangle$, and $|0, 8\rangle$, for $|0, 19\rangle$ the basis states $|0, 20\rangle$, $|0, 19\rangle$, $|0, 18\rangle$, and $|0, 17\rangle$, and for $|9, 19\rangle$ the basis states $|9, 20\rangle$, $|9, 19\rangle$, $|9, 18\rangle$, and $|9, 17\rangle$. Both for superposition and mixture of basis states, the results are qualitatively similar to those shown in Fig.14.26. Therefore we expect that some imprecision in exciting an initial state in the junctions would not affect in a relevant way the results. we may also conclude, that the excitation of QB states does not rely on the phase coherence.

Let us estimate how many quanta should be excited in the junctions in order to obtain QBs (tunneling pairs). We compute the density $\rho(n_1, n_2) = |\langle n_1, n_2 | \chi \rangle|^2$ of the asymmetric state $|\chi\rangle = (|\chi_b^{(S)}\rangle + |\chi_b^{(A)}\rangle)/\sqrt{2}$, where $|\chi_b^{(S,A)}\rangle$ are the eigenstates belonging to a tunneling pair [29]. In Fig. 14.27 we show a contour plot of the logarithm of the density for the tunneling pair with energy marked by the arrow labeled by number two in Fig. 14.25-(b).

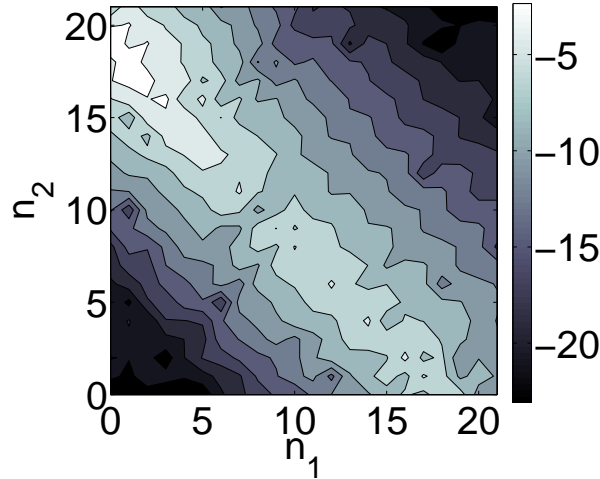


Figure 14.27: Contour plot of the logarithm of the density of the asymmetric state $|\chi\rangle = (|\chi_b^{(S)}\rangle + |\chi_b^{(A)}\rangle)/\sqrt{2}$ as a function of the number of quanta at junctions 1 and 2 (see text). The parameters are $\gamma = Ib/Ic = 0.945$ and $\zeta = 0.1$ (22 levels per junction).

We see that the density has its maximum around $n_1 = 19$ and $n_2 = 0$ which is consistent with the result shown in Fig. 14.26-c and d where QBs were excited by using this combination of quanta in the junctions.

14.7 Experimental realizations

There is a fast growing amount of experimental and related theoretical work on applying the quantum discrete breather concept to many different branches in physics, like Bose-Einstein condensates, crystals and molecules, surfaces, and others. We will discuss some of these at length, while others will be reviewed more briefly.

14.7.1 Repulsively bound atom pairs

Winkler et al [53] performed experiments with a three-dimensional optical lattice with initially each site being either not occupied, or being occupied by two Rb atoms bound in a pair due to attractive interaction. A magnetic field sweep across the Feshbach resonance changes the sign of interaction, turning attraction into repulsion. The dynamics of ultracold atoms loaded into the lowest band of the optical potential is described by the quantum DNLS model, which is equivalent to the Bose-Hubbard model (14.10). Lifetime measurements have shown, that repulsive pairs of Rb atoms have larger lifetimes than pairs of weakly or almost not interacting atoms (Fig.14.28). The two-particle bound states discussed in chapter 14.2.1

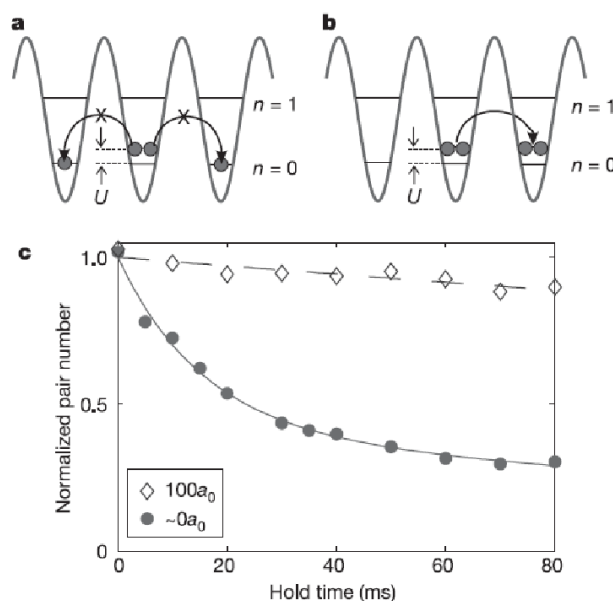


Figure 14.28: (a) Repulsive interaction between two atoms sharing a lattice site gives rise to an interaction energy U . Breaking up of the pair is suppressed owing to the lattice band structure and energy conservation. This is the simplest version of a quantum discrete breather. (b) The discrete breather can tunnel along the lattice. (c) Long lifetimes of strongly repulsive atoms. The plot shows the remaining fraction of pairs for strong interaction (open diamonds) and for almost vanishing interaction (filled circles). Adapted from [53].

- the simplest versions of a quantum discrete breather - are the obvious explanation of the experimental findings. Indeed, neglecting Landau-Zener transitions to higher lying bands in the optical potential, the Bose-Hubbard model is justified. The sign of the interaction does not play any role, since it only changes quantum discrete breathers from being low-lying to being excited states, not affecting their localization properties. The most simple argument of why two quanta (or atoms) placed initially close to each other, do not separate despite they repel each other, is based on the fact, that if they would do so, the (large) interaction energy should be converted into kinetic energy, which is restricted to be less than two times the width of the single particle band. In other words, repulsively bound atom pairs are a straightforward consequence of quantum discrete breather states with two quanta.

Another sophisticated experimental investigation aimed at measuring the quasi-momentum distribution of atom pairs in various regimes by mapping it onto a spatial distribution, which was finally measured using standard absorption imaging (Fig.14.29). Therefore predictions of such states, which were made more than 30 years ago by Ovchinnikov [54], were beautifully confirmed experimentally with ultracold repulsive atoms.

14.7.2 Molecules

Intramolecular vibrational energy redistribution (IVR) has been a central issue in the field of chemical physics for many decades. In particular, pathways and rates are of importance there, since understanding them allows to describe e.g. the dynamics of various chemical

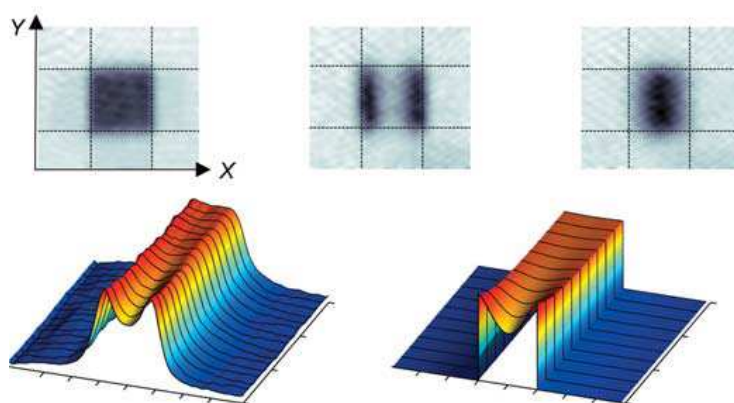


Figure 14.29: (Upper row) Absorption images of the atomic distribution after release from the 3D lattice and a subsequent 15 ms time of flight. The horizontal and vertical black lines enclose the first Brillouin zone. (upper left) Lattice sites are occupied by single atoms; (upper middle) Repulsively bound atom pairs; (upper right) Attractively bound atom pairs; (bottom row) Quasi-momentum distribution for pairs in one direction as a function of the lattice depth after integrating out the other direction. (bottom left) Experiment; (bottom right) Numerical calculations. Adapted from [53].

reactions, and dissociation processes [55]. Spectroscopical studies, where single vibrational quanta are excited, allow to measure the frequencies of normal vibrational modes, i.e. to characterize the dynamics of a molecule for small amplitude vibrations. These normal modes consist of coherent combinations of vibrational excitations of several bonds (or rotational groups) in a molecule. However, in order e.g. to dissociate a molecule, a many quanta excitation is needed, and nonlinearities will certainly become important. It was realized then, that strong vibrational excitations of molecules are much better described by so-called *local modes*, i.e. basically one or few bond vibrational excitations. That transition from normal to local modes remained a puzzle for a long time. A practically complete modern theoretical account on these issues can be found in a recent monography by Ovchinnikov, Erikhman and Pronin [56]. On its most abstract level, the transition from normal to local modes is identical with the bifurcation in the dimer model. Thus, local modes are essentially discrete breathers or slight perturbations of them. Note, that the connection between local modes, breathers and periodic orbits has been recently studied by Farantos in the context of large biological molecules [57]. Discrete breathers (ILMs) have been theoretically predicted to exist in ionic crystals [58], ways of optical excitation of DBs (ILMs) have been proposed [59], and their possible presence in hydrocarbon structures has been discussed [60].

Exciting local modes in molecules with discrete symmetries leads to small tunneling splittings of excitation levels [56], and goes back to the work of Child and Lawton [61], see also a recent comprehensive review by Keshavamurthy [62] and references therein. On its most abstract level, this effect is identical with the tunneling splitting in the permutationally symmetric dimer model discussed in chapter 14.2.2.

An early example of experimental evidence of discrete breather excitations in molecules comes from spectroscopical studies of visible red absorption spectra of benzene, naphthalene, and anthracene by Swofford et al [64]. The C-H stretching vibrations have been excited

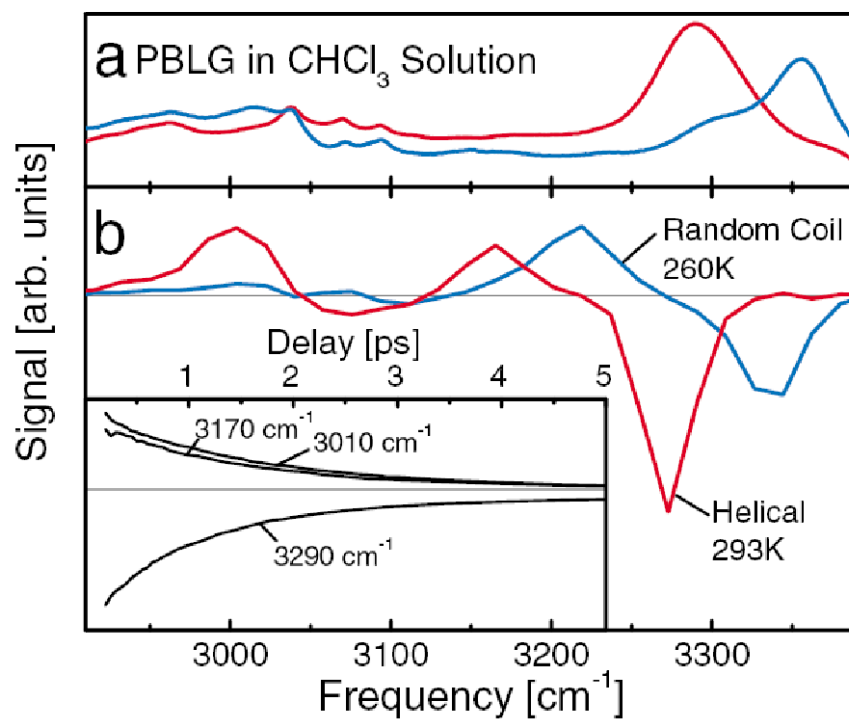


Figure 14.30: (a) Absorption spectra of PBLG in chloroform at 293 K (red line, helical conformation) and at 260 K (blue line, random coil). (b) Pump-probe spectra 600 fs after excitation under the same conditions. Inset: Decay of negative and both positive bands at 293 K. Adapted from [63].

to the sixth quantum level, and red shifts of the lines show, that instead of a delocalized excitation of six bonds to the first level (yielding six quanta), the excitation resides on just one of the six available bonds. While it can tunnel (as a quantum discrete breather) to the other bonds, this tunneling time is a new large time scale in the problem, strongly affecting e.g. dissociation rates.

A recent study of femtosecond infrared pump-probe spectroscopy of the N-H mode of a stable α -helix (poly- γ -benzyl-L-glutamate (PBLG)) revealed two excited-state absorption bands, which disappear upon unfolding of the helix [63]. PBLG forms extremely stable, long α -helices in both helicogenic solvents and films grown from these solvents. The monomeric unit of PBLG is a non-natural amino-acid with a long side chain that stabilizes the helix. PBLG has served as the standard model helix since the very early days of structural investigations of proteins. Fig.14.30(a) (red line) shows the absorption spectrum of the helix at 293 K, which is dominated by the strong N-H stretching band at 3290 cm⁻¹. Fig.14.30(b) (red line) shows the pump-probe response 600 fs after excitation with an ultrashort broadband pulse. One negative (3280 cm⁻¹) and two positive bands (3160 and 3005 cm⁻¹) are observed. If the N-H stretching modes were isolated, a negative band associated with bleach and stimulated emission, and a positive band associated with excited-state absorption, would be expected. This is indeed observed here for the unfolded molecule. In contrast, the observation of *two* positive bands for the intact helix rather than just one, is exceptional. Edler et al [63] argue, that these features can not be explained due to intensity dependencies, or

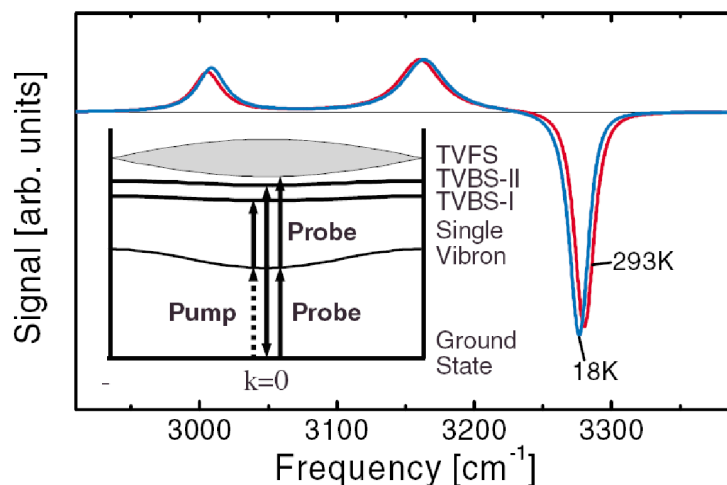


Figure 14.31: Simulated pump-probe spectrum for 293 K (red line) and 18 K (blue line). Inset: schematic of the energy levels. Adapted from [63].

Fermi resonances. A consistent explanation is reached by assuming that two vibron states are excited, and these vibrons may form two different types of bound states, self trapped either on the same site, or on neighbouring ones. The latter states originate from the acoustic phonons of the helix, which correlate adjacent sites (see also [65]).

14.7.3 Crystal surfaces

Depositing atoms or molecules on crystal surfaces can be controlled experimentally, and as a result a planar regular two-dimensional lattice structure of the deposited material can be obtained. Guyot-Sionnest [66] used Hydrogen to be deposited on Si(111) surfaces. The Si-H bonds can be excited using pump-probe techniques with infrared dye lasers. There is substantial interaction between the Si-H bonds on the Si(111) surface. The pump excites one phonon (quantum), while the tunable probe frequency finds a substantial red shift of the two-phonon excitation, and allows to conclude, that two-phonon bound states are observed.

Another set of experiments was performed by Jakob [67–69]. Carbon monoxide (CO) was deposited on a Ru(001) single crystal surface. The C-O stretching modes constitute a two-dimensional array of weakly interacting anharmonic oscillators with 4.7 Å intermolecular distance. Intermolecular coupling is provided by means of the electric field of the oscillating dipoles. Experimental spectra at 30 K are shown in Fig.14.32. The one phonon mode frequency is at 2031 cm⁻¹. This has to be compared to the naturally abundant ¹³C¹⁶O frequency at 1941 cm⁻¹. The corresponding blue shift for the adsorbate is thus due to additional stiffness provided by the Ru surface coupling. Excitation of two uncorrelated phonons would yield a two phonon continuum at about 4062 cm⁻¹. The narrow line observed at 3940 cm⁻¹ can be thus attributed to a two-phonon bound state, or a quantum discrete breather excitation.

The temperature dependence of the line positions also clearly shows, that the two-phonon

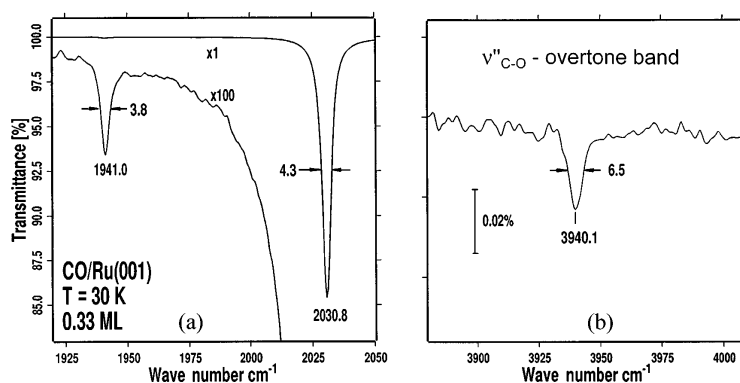


Figure 14.32: (a) Infrared absorption spectra of the C-O stretching mode at 30 K. The corresponding mode of naturally abundant $^{13}\text{C}^{16}\text{O}$ is displayed in an enlarged vertical scale; (b) the overtone band observed at less than twice the frequency of the fundamental mode. Adapted from [67].

bound state line softens much slower than the line of the one-phonon delocalized state (Fig.14.33). This is, among other facts, a strong indication that the observed red shift

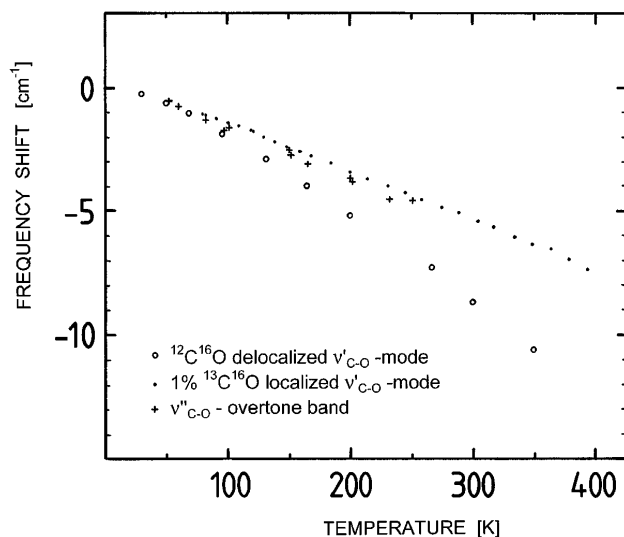


Figure 14.33: Frequency shifts of the vibrational bands with temperature: crosses - overtone band, dots - fundamental of naturally abundant $^{13}\text{C}^{16}\text{O}$, open circles - delocalized fundamental of $^{12}\text{C}^{16}\text{O}$. Adapted from [67].

of the overtone line is due to the formation of a localized two-phonon bound state, or a (quantum) discrete breather.

In the bulk of solids

Vibrational spectra in the overtone or combination region of molecular crystals have been studied intensively in the 1970s and 1980s. A pioneering theoretical proposal was due to

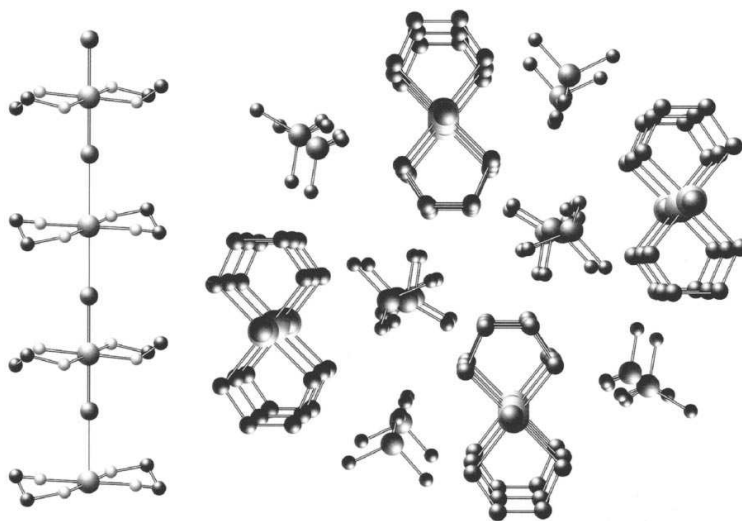


Figure 14.34: Structure of the PtCl crystal. One PtCl chain is shown on the left. Each Pt atom is coordinated by two ethylenediamine units in a near square planar geometry, while Cl ions connect Pt sites along the chain. The packing arrangement of the 1D chains and their ClO_4^- counterions is shown on the right. Adapted from [76].

Agranovich, who predicted the existence of two-exciton bound states in various molecular crystal materials [70]. Experimental studies of infrared absorption spectra for CO_2 crystals were conducted by Dows et al [71] and gave evidence of two-phonon bound states. Dressler et al studied the slow vibrational relaxation of N_2 , which also indicates the presence of many-phonon bound states [72]. In a remarkable theoretical paper, Bogani calculated the spectrum of two phonon excitations in molecular crystals [73], to some extent one of the first accurate calculations of quantum discrete breathers. More recently Bini et al reconsidered the theory of three-phonon bound states in crystal CO_2 [74]. While there certainly are many other results worth to be mentioned, we recommend reading related chapters in [75], [56].

The pioneering studies of Swanson et al [76] have shown that up to seven phonons can bind and form a localized state. The system of choice was a PtCl based crystal - a halide-bridged mixed-valence transition metal complex, which is a model low-dimensional electronic material where the ground states can be systematically tuned (with chemistry, doping, pressure, and temperature). It is a very strong charge-density wave (CDW) example. The material is a well-formed crystal with a homogeneous lattice consisting of quasi-1D chains (see Fig.14.34). The CDW ground state consists of alternating Pt^{+2} and Pt^{+4} sites with a corresponding distortion of the chloride ions towards the Pt^{+4} site. Resonance Raman spectra were used to probe both ground and photoexcited states. They probe the fundamental Cl-Pt-Cl stretch and the progression of many overtones. At low temperatures, the fundamental exhibits a fine structure with up to six discrete, well-resolved modes. The analysis of the evolution of the spectral structure in the overtones was performed for isotopically pure samples, in order to avoid exciting localized states due to isotopic disorder. The fundamental and overtone spectra for the pure Pt^{35}Cl sample are shown in Fig.14.35. The data are presented in a stack plot in which each successive trace is offset along the horizontal axis by increasing multiples of the fundamental frequency 312 cm^{-1} . Such plots clearly expose the relation of features in the overtone spectrum to multiples of the fundamental peak. The lowest energy dominant feature in each trace (marked by vertical lines) demonstrates a strongly increasing anharmonic redshift. Further, at higher overtones, each of these dominant peaks recurs, offset

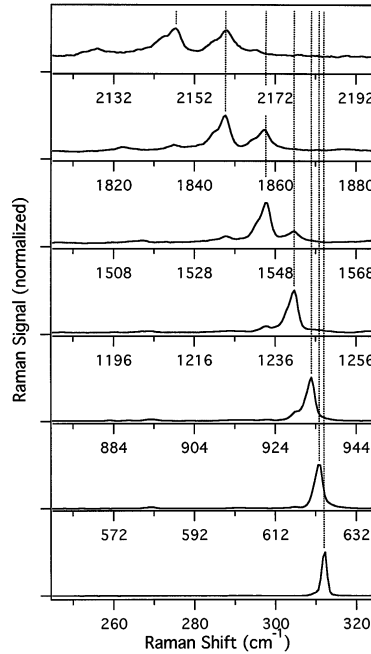


Figure 14.35: Fundamental and overtone spectra of isotopically pure Pt^{35}Cl . Moving upward in each panel, each x axis is offset by the appropriate integral multiple of the 312 cm^{-1} fundamental frequency. All spectra have been scaled vertically to equal peak intensities. Adapted from [76].

by the fundamental frequency, in the next trace above. A simple interpretation is that the lowest-energy dominant peaks in the overtone spectra correspond to all quanta of vibrational energy localized in approximately one PtCl_2 unit, while the higher energy peaks correspond to having all quanta but one in a localized PtCl_2 unit combined with one quanta in the more extended fundamental. The schematic process of the energy transfer is shown in Fig.14.36 and has been analyzed theoretically in [77].

An incoming photon at frequency ν is exciting an electron from a Pt^{+2} to a Pt^{+4} site. The Cl ion between them starts oscillating. Finally the electron relaxes back to its original position, and releases a photon with frequency ν' . The energy difference is remaining in a localized vibration. The effect of isotope disorder was treated by Kalosakas et al [78]. The experimentally observed redshifts were also theoretically described by Fehske et al [79] using Peierls-Hubbard models, and by Wellein et al using the Holstein model [80].

Inelastic X-ray and neutron scattering was used by Manley et al [81–83] to probe phonon dispersion in α -uranium single crystals. Variation of temperature showed softening, and the abrupt appearance of a new dynamical mode, without a typically observed phase transition. The authors argue that this mode is a discrete breather, and forms due to strong electron-phonon interaction.

Russell and Eilbeck reported evidence for moving breathers in the layered crystal muscovite at 300 K [84]. Breathers were created by bombardment of the crystal surface with heavy ions. Ejection of atoms at the opposite (shielded) crystal surface was attributed to breathers, which were able to carry the vibrational energy without dispersing over more than

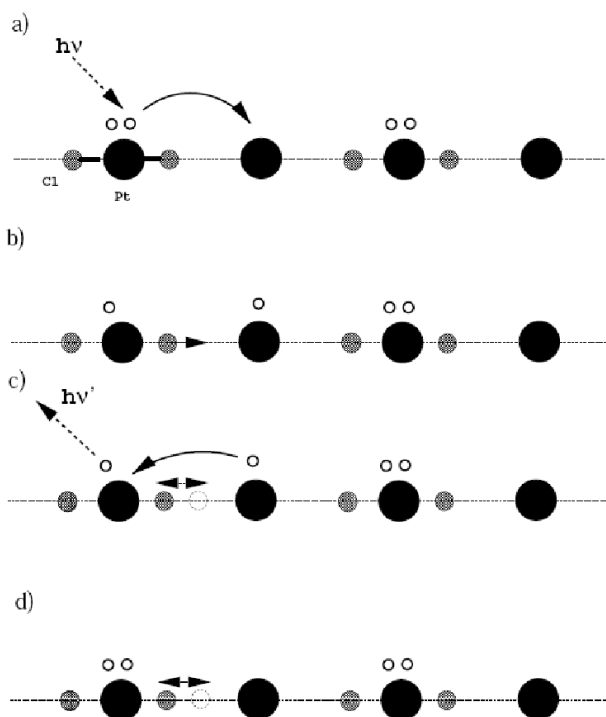


Figure 14.36: A simple picture of a resonant Raman scattering event in the localized atomic limit. Large filled circles mark Pt ions, small grey circles mark Cl ions. Open circles mark the positions of electrons. Adapted from [77].

10^7 unit cells of the crystal.

Finally Abramosis et al [85] reported on anomalous bulk diffusion of interstitial Nitrogen in steel microcrystals. N ions were deposited in a micron-thick layer, and are trapped by local structures, with a characteristic binding energy. Ar ion bombardment increases the N mobility at depths far beyond the ion penetration depth. The authors see evidence for coherent transfer of vibrational energy deep into the bulk of the material.

14.8 Conclusions and outlook

Progress in the understanding of classical discrete breathers evolved for two decades, and has significantly improved our understanding of the complexity in the dynamics of anharmonic lattice dynamics. The little input it needs to form discrete breathers - spatial discreteness and nonlinearity - were demonstrated to generate an impressive list of experimental observations in a large variety of different physical systems, with length and time scales ranging over many orders of magnitude. The quantization of the classical equations of motion opened a whole new avenue of research on quantum breathers. For obvious computational reasons numerical studies are much more involved in the quantum domain, restricting our potential of detailed understanding to either small lattices, or few participating quanta. Nevertheless, a set of experiments, comparable in size to its classical counterpart, has been reviewed

where quantum breathers are detected. Still we anticipate this only to be the beginning of a much more sophisticated undertaking. We may expect many new qualities to show up in the regime of large lattices and many participating quanta. These limits are conceptually closing the gap to quantum interacting many body problems, which are at the heart of condensed matter physics, and quantum computing. Yet another highly interesting, complicated and debated problem is the combined influence of discreteness, nonlinearity, and disorder. Linear disordered wave equations allow for Anderson localization. It is a thrilling modern theme to study the constructive and destructive interplay of all three ingredients. The best is yet to come.

References

- [1] P.W. Anderson, Phys. Rev. **109**, 1492 (1958).
- [2] S. Flach and C. R. Willis, Phys. Rep. **295**, 181 (1998).
- [3] D. K. Campbell, S. Flach, Y. S. Kivshar, Physics Today **57** (1) pp. 43-49 (2004).
- [4] S. Flach and A. V. Gorbach, Phys. Rep. **467**, 1 (2008).
- [5] S. Flach and A. V. Gorbach, Chaos **15**, 015112 (2005).
- [6] M. Eleftheriou and S. Flach, Physica D **202** 142 (2005).
- [7] S. Aubry, Physica D **103**, 201 (1997).
- [8] R. S. MacKay, Physica A **288** 174 (2000).
- [9] V. Fleurov, Chaos **13**, 676 (2003).
- [10] W. Z. Wang, J. Tinka Gammel, A. R. Bishop and M. I. Salkola, Phys. Rev. Lett. **76**, 3598 (1996).
- [11] S. A. Schöefield, R. E. Wyatt and P. G. Wolynes, J. Chem. Phys. **105** 940 (1996).
- [12] P. D. Miller, A. C. Scott, J. Carr and J. C. Eilbeck, Phys. Scr. **44** 509 (1991).
- [13] A. C. Scott, J. C. Eilbeck, and H. Gilhøj, Physica D **78**, 194 (1994).
- [14] J. C. Eilbeck, in *Localization and Energy Transfer in Nonlinear Systems*, edited by L. Vazquez, R. S. MacKay, and M. P. Zorzano (World Scientific, Singapore, 2003), p. 177.
- [15] L. Bernstein, J. C. Eilbeck, and A. C. Scott, Nonlinearity **3**, 293 (1990).
- [16] L. J. Bernstein, Physica D **68**, 174 (1993).
- [17] S. Aubry, S. Flach, K. Kladko, and E. Olbrich, Phys. Rev. Lett. **76**, 1607 (1996).
- [18] G. Kalosakas, A. R. Bishop, Phys. Rev. A **65**, 043616 (2002).
- [19] S. Flach and V. Fleurov, J. Phys.: Cond. Matt. **9**, 7039 (1997).
- [20] S. Flach, V. Fleurov, and A. A. Ovchinnikov, Phys. Rev. B **63**, 094304 (2001).
- [21] R. A. Pinto and S. Flach, Phys. Rev. A **73**, 022717 (2006).
- [22] J. Dorignac and S. Flach, Phys. Rev. B **65**, 214305 (2002).
- [23] L. Proville, Phys. Rev. B **71**, 104306 (2005).
- [24] L. Proville, Phys. Rev. B **72**, 184301 (2005).
- [25] L. Proville, Europhys. Lett. **69**, 763 (2005).
- [26] V. Fleurov, R. Schilling and S. Flach, Phys. Rev. E —bf **58**, 339 (1998).
- [27] G. Kalosakas, A. R. Bishop, V. M. Kenkre, J. Phys. B **36**, 3233 (2003).
- [28] R. A. Pinto and S. Flach, EPL **79**, 66002 (2007).
- [29] R. A. Pinto and S. Flach, Phys. Rev. B **77**, 024308 (2008).
- [30] S. Flach, V. Fleurov, and A. V. Gorbach, Phys. Rev. B **71**, 064302 (2005).
- [31] L. S. Schulman, D. Tolkunov, E. Mihokova, Phys. Rev. Lett. **96**, 065501 (2006); Chem. Phys. **322**, 55 (2006); L.S. Schulman, D. Tolkunov, E. Mihókova, Chem. Phys **322**, 55 (2006).
- [32] L. Proville, Physica D **216**, 191 (2006).
- [33] A. P. Tonel, J. Links, and A. Foerster, J. Phys. A: Math. Gen. **38**, 1235 (2005).
- [34] L. B. Fu and J. Liu, Phys. Rev. A **74**, 063614 (2006).

- [35] T.-C. Wei and P. M. Goldbart, Phys. Rev. A **68**, 042307 (2003).
- [36] A. Shimony, Ann. NY. Acad. Sci. **755**, 675 (1995).
- [37] H. Barnum and N. Linden, J. Phys. A.: Math. Gen. **34**, 6787 (2001).
- [38] A. P. Hines, R. H. McKenzie, and G. J. Milburn, Phys. Rev. A **67**, 013609 (2003).
- [39] K. G. Makris, S. Suntsov, D. N. Christodoulides, G. I. Stegeman, and A. Hache, Opt. Lett. **30**, 2466 (2005); M. Molina, I. L. Garanovich, A. A. Sukhorukov, and Yu. Kivshar, Opt. Lett. **31**, 2332 (2006).
- [40] M. I. Molina, R. A. Vicencio, and Y. S. Kivshar, Opt. Lett., **31**, 1693 (2006).
- [41] S. Suntsov, *et al*, Phys. Rev. Lett. **96**, 063901 (2006); E. Smirnov *et al*, Opt. Lett. **31**, 2338 (2006), C. R. Rosberg *et al*, Phys. Rev. Lett. **97**, 083901 (2006).
- [42] V. Pouthier, Phys. Rev. B **76**, 224302 (2007).
- [43] R. A. Pinto, M. Haque and S. Flach, Phys. Rev. A **79**, 052118 (2009).
- [44] J.-P. Nguenang and S. Flach, Phys. Rev. A **80**, 015601 (2009).
- [45] M. A. Baranov, Phys. Rep. **464**, 71 (2008).
- [46] R. McDermott *et al*, Science **307**, 1299 (2005); M. Steffen *et al*, Science **313**, 1423 (2006).
- [47] *Quantum Computing and Quantum Bits in Mesoscopic Systems*, edited by A. Leggett, B. Ruggiero, and P. Silvestrini (Kluwer Academic/Plenum Publishers, New York, 2004).
- [48] *Les Houches 2003, Quantum Entanglement and Information Processing*, edited by D. Estève, J. M. Raimond, and J. Dalibard (Elsevier, Amsterdam, 2004).
- [49] J. Q. You and F. Nori, Physics Today, November (2005).
- [50] M. Davis, E. Heller, J. Chem. Phys. **75**, 246 (1981).
- [51] S. Keshavamurthy, Int. Rev. Phys. Chem. **26**, 521 (2007).
- [52] S. Keshavamurthy, J. Chem. Phys. **122**, 114109 (2005).
- [53] K. Winkler, G. Thalhammer, F. Lang, R. Grimm, J. Ecker Denshlag, A. J. Daley, A. Kantian, H. P. Büchler, and P. Zoller, Nature **441**, 853 (2006).
- [54] A. A. Ovchinnikov, Zh. Eksp. Teor. Fiz. / Soviet Phys. JETP **57/30:263**, 147 (1969/1970).
- [55] M. Joyeux, S. Yu. Grebenshchikov, J. Bredenbeck, R. Schinke, S. C. Farantos, Adv. Chem. Phys. **130**, 267 (2005).
- [56] A. A. Ovchinnikov, N. S. Erikhman and K. A. Pronin, *Vibrational-Rotational Excitations in Nonlinear Molecular Systems*, Kluwer Academic/Plenum Publishers (2001).
- [57] S. C. Farantos, J. Chem. Phys. **126**, 175101 (2007).
- [58] S. A. Kisilev, A. J. Sievers and G. V. Chester, Physica D **123**, 393 (1998).
- [59] T. Rössler and J. B. Page, Physica B **220**, 387 (1996); Phys. Rev. Lett. **78**, 1287 (1997); Phys. Rev. B **62**, 11460 (2000).
- [60] G. Kopidakis, S. Aubry, Physica B **296**, 237 (2001).
- [61] M. S. Child, R. T. Lawton, Chem. Phys. Lett. **87**, 217 (1982).
- [62] S. Keshavamurthy, Int. Rev. Phys. Chem. **26**, 521 (2007).
- [63] J. Edler, R. Pfister, V. Pouthier, C. Falvo, P. Hamm, Phys. Rev. Lett. **93**, 106405 (2004).
- [64] R. L. Swofford, M. E. Long, A. C. Albrecht, J. Chem. Phys. **65**, 179 (1976).
- [65] P. Hamm, J. Edler, in: T. Dauxois, A. Litvak-Hinenzon, R. MacKay, A. Spanoudaki (Eds.), *Energy Localization and Transfer*, World Scientific, Singapore, (2004).
- [66] P. Guyot-Sionnest, Phys. Rev. Lett. **67**, 2323 (1991).
- [67] P. Jakob, Phys. Rev. Lett. **77**, 4229 (1996).
- [68] P. Jakob, Physica D **119**, 109 (1998).
- [69] P. Jakob, Surface Science **428**, 309 (1999).
- [70] V. M. Agranovich, Sov. Phys.-Solid St. **12**, 438 (1970).
- [71] D. A. Dows, V. Schettino, J. Chem. Phys. **58**, 5009 (1973).
- [72] K. Dressler, O. Oehler, D. A. Smith, Phys. Rev. Lett. **34**, 1364 (1975).
- [73] F. Bogani, J. Phys. C.: Solid State Phys. **11**, 1283 (1978).

- [74] R. Bini, P. R. Salvi, V. Schettino, H. J. Jodl, J. Chem. Phys. **98**, 164 (1993).
- [75] V. M. Agranovich, R. M. Hochstrasser, *Spectroscopy and excitation dynamics of condensed molecular crystals*, North-Holland, Amsterdam (1983).
- [76] B. I. Swanson, J. A. Brozik, S. P. Love, G. F. Strouse, A. P. Shreve, A. R. Bishop, W.-Z. Wang, M. I. Salkola, Phys. Rev. Lett. **82**, 3288 (1999).
- [77] K. Kladko, J. Malek, A. R. Bishop, J. Phys.: Condens. Matter **11**, L415 (1999).
- [78] G. Kalosakas, A. R. Bishop, A. P. Shreve, Phys. Rev. B **66**, 894303 (2002).
- [79] H. Fehske, G. Wellein, H. Buettner, A. R. Bishop, M. I. Salkola, Physica B **281**, 673 (2000).
- [80] G. Wellein, H. Fehske, Phys. Rev. B **58**, 6208 (1998).
- [81] M. E. Manley, M. Yethiraj, H. Sinn, H. M. Volz, A. Alatas, J. C. Lashley, W. L. Hulst, G. H. Lander, J. L. Smith, Phys. Rev. Lett. **96**, 125501 (2006).
- [82] M. E. Manley, M. Yethiraj, H. Sinn, H. M. Volz, A. Alatas, J. C. Lashley, W. L. Hulst, G. H. Lander, D. J. Thoma, J. L. Smith, J. Alloys and Comp. **444-445**, 129 (2007).
- [83] M. E. Manley, J. W. Lynn, Y. Chen, G. H. Lander, Phys. Rev. B **77**, 852301 (2008).
- [84] F. M. Russell, J. C. Eilbeck, EPL **78**, 10004 (2007).
- [85] G. Abrasonis, W. Moeller, X. X. Ma, Phys. Rev. Lett. **96**, 065901 (2006).

